Evolutionary developmental biology of bitterling fish

Yi, W.

Chapter 3 Developmental neuroanatomy of the rosy bitterling *Rhodeus ocellatus* (Teleostei: Cypriniformes)

Wenjing Yi[1], Thomas Mueller[2], Martin Rücklin[3], and Michael K. Richardson[1]

1, Institute of Biology, University of Leiden, Sylvius Laboratory, Sylviusweg 72, 2333BE, Leiden, the Netherlands.

2, Division of Biology, Kansas State University, 340 Ackert Hall, Manhattan, KS 66506-4901, Kansas, United States.

3, Vertebrate Evolution, Development and Ecology, Naturalis Biodiversity Center, Postbus 9517, 2300 RA Leiden, The Netherlands.

Manuscript under revision at *Journal of Comparative Neurology*

Abstract

Bitterlings are a group of teleost fish (Cyprinifromes: Acheilanathidae) that notable for their brood parasitic lifestyle. Bitterling embryos develop as parasites inside the gill chamber of their freshwater mussel hosts. However, little is known about brain development of this valuable model for evolutionary adaptation of parasitism. Here, we have imaged the development of the brain of the rosy bitterling, *Rhodeus ocellatus*, at four embryonic stages of 165, 185, 210, 235 *hpf* using micro-Computed tomography (microCT) with a specific focus on developmental regionalization and brain ventricular organization. We have given a detailed neuroanatomical account of the development of the brain divisions with reference to The *Atlas of Early Zebrafish Brain Development* and the prosomeric model. Segmentation and three-dimensional visualization of the ventricular system were performed in order to clarify changes in the longitudinal brain axis as a result of cephalic flexure during development. The results show that during early embryonic and larval development, histological differentiation, tissue boundaries, periventricular proliferation zones, and ventricular spaces are all detectable by microCT. Importantly, our approach is validated by the fact that the profile of CT values displayed here in the bitterling brain are consistent with genoarchitecture identified in previous neurodevelopmental. Distinct developmental heterochrony of the precocious development of the inferior lobe are seen in the rosy bitterling compared to the zebrafish.

Introduction

Bitterlings, a group of freshwater teleosts, have been established as valuable model species in behavioral, population and evolutionary ecology due to their brood parasitic life history. Their peculiar life style involves the laying of eggs by the bitterling in a host mussel, a phenomenon that has been recognized for more than a century (Boeseman et al., 1938; Chang, 1948; Duyvené de Wit, 1955; Kitamura et al., 2012; Mills and Reynolds, 2003; Olt, 1893; Reichard et al., 2007; Rouchet et al., 2017; Smith, 2016; Wiepkema, 1962). Noll (1877) was the first to show that the embryos of European bitterling (*Rhodeus amarus*) develop in the gill chamber of their host mussel. This location provides a sheltered environment which protects the developing embryos from potential predators (Aldridge, 1999; Liu et al., 2006; Reichard et al., 2007; Smith et al., 2004). We (Yi et al., 2021) have recently compared developmental sequences of the rosy bitterling (*Rhodeus ocellatus*) to the zebrafish (*Danio rerio*); the latter is a non-parasitic teleost which lays its eggs into the open water (Kimmel et al., 1995; Lawrence, 2007). That study confirmed the relative pre-displacement of hatching, and the relative delay of development of the pectoral fins, in the bitterling.

The specialized ontogeny of the bitterling, and its brood parasitic lifestyle, make it a potentially interesting model for the study of developmental mechanisms underlying brain evolution. In this study, we generated an atlas of the developing bitterling brain as a reference for cross-species comparisons. To build a foundation for such comparisons, we related the bitterling brain development with published data of the zebrafish. The comparison to the zebrafish is useful for two reasons: Firstly, the zebrafish is firmly established as a genetic model system that has been most thoroughly investigated with regard to embryonic, postembryonic, and larval stages (Mueller and Wullimann, 2003; Mueller and Wullimann, 2016; Mueller et al., 2006; Wullimann, 2009; Wullimann and Knipp, 2000; Wullimann and Mueller, 2004). Secondly, both, the bitterling and the zebrafish belong to the group of carp-like (cyprinid) teleosts with very similar adult brain anatomy yet, as we show, distinct developmental heterochronies. A developmental stage atlas of the bitterling brain as visualized in this study, provides a foundation to examine the molecular mechanisms underlying these heterochronies.

In the vertebrates, the central nervous system, including its anteriormost part, the brain, develops from the neural tube (Richardson and Wright, 2003; Schmitz et al., 1993; Wullimann, 2009). In teleosts, including bitterlings, the development of the neural tube involves secondary neurulation (Schmitz et al., 1993). The definitive neural tube is filled with cerebrospinal fluid (Lowery and Sive, 2009). The neural tube caudal to the brain is the spinal cord, and has a narrow lumen called the central canal. The brain has an inflated, irregular lumen which form a series of brain ventricles (Korzh, 2018). In general, the vertebrate brain consists of four parts: (1) the secondary prosencephalon, (2) the diencephalon, (3) the mesencephalon, and (4) the rhombencephalon. Correspondingly, the brain ventricular system has been divided into the 4th ventricle (the lumen of the rhombencephalon); the mesencephalic ventricle; the 3rd ventricle (the lumen of diencephalon proper); and the prosencephalic ventricle (including the telencephalic ventricle and the hypothalamic part of the classic diencephalic ventricle; Nieuwenhuys and Puelles, 2016).

In this study we used the prosomeric model of Puelles and Rubenstein (2003) for dividing neuromeres in the secondary prosencephalon as well as for defining other brain divisions. In general, the prosomeric model alongside its recognition of longitudinal zones and transverse neuromeres forms a powerful paradigm for vertebrate cross-species comparisons. One reason for this is that the

model is based on conserved molecular and developmental characteristics that allow a consistent demarcation of the CNS into developmental units (morphogenetic entities) along the neuraxis of a range of vertebrate species. Applying the prosomeric model for the development of the zebrafish brain, it has been demonstrated that cellular processes, i.e., proliferation, migration and differentiation, can used to define prosomeric units in teleosts (Mueller and Wullimann, 2003; Mueller and Wullimann, 2016; Mueller et al., 2006; Wullimann, 2009; Wullimann and Knipp, 2000; Wullimann and Mueller, 2004).

The prosomeric model analyzes brain regions along the general brain axis and according to the mediolateral extent of brain regions. Longitudinally, the neural tube has four compartments divided by the *sulcus limitans* that was first defined by Wilhelm His, Sr. (His Wilhelm, 1895); reviewed by Puelles (2019). The four compartments are: the roof plate dorsally, the alar plate dorsolaterally, the basal plate ventrolaterally, and the floor plate ventrally.

According to Nieuwenhuys and Puelles (2016), the rhombencephalon consists of twelve neuromeres (rhombomeres, isthmus or r0 plus r1-r11) in longitudinal series. In cyprinids like the Goldfish (*Carassius auratus*), the rostral rhombomeres two to six (r2-r6) correspond to the mammalian pons, whereas the caudal rhombomeres seven to eight (r7-8) correspond to the mammalian medulla oblongata (Gilland et al., 2014; Rahmat and Gilland, 2019). The rostral rhombomeres r2-r6 form clearly segmented neural clusters while the caudal r7-r8 lack a precise morphological delineation (Ma et al., 2009). The zebrafish r8 is twice as large as the rostral rhombomeres, composed by multiple crypto- or pseudo rhombomeres that can be delimited only molecularly similar to the avian brain (Cambronero and Puelles, 2000). The rostral subdivision of neuromeres is more complex, because bending of the neural tube (the cephalic flexure, Hauptmann and Gerster, 2000; Mueller and Wullimann, 2009) has made the definition of the longitudinal neuraxis more difficult (Mueller and Wullimann, 2009; Puelles, 2019; Vernier, 2017; Wullimann and Rink, 2002).

Here, we visualize the development of the rosy bitterling (*Rhodeus ocellatus*) brain using micro-Computed tomography (microCT, x-ray microscopy or µCT) with a specific focus on developmental regionalization and brain ventricular organization. MicroCT is a widely used high-resolution, non-destructive, three-dimensional (3D) imaging technique (Babaei et al., 2016; Metscher, 2009a) that just recently has been introduced to study development (Wong et al., 2015). The contrast of CT scans is based on absorption of x-ray radiation passed through the sample. Conventionally, highly mineralized structures like bones and teeth have higher attenuation coefficient (CT value or Hounsfield units), and are brighter and easier to recognize than soft tissues. For the visualization of the latter, a treatment with contrast agents is needed. In this work, we used phosphotungstic acid (Metscher, 2009b), which allows discrimination of soft tissues such as muscles, nerves, and blood vessels. In this study, we extend MicroCT techniques to the developing fish brain. Our goal is to establish microCT and 3D visualizations as complementary methods for cross-species comparisons of structural characteristics of both developing and mature brains. In fact, our results indicate that microCT is useful to quantitatively analyze, for example, ventricular spaces, and white matter versus proliferative and postmitotic cell masses.

Materials and Methods

Sample preparation

Embryos of six developmental stages of 135, 150, 165, 185, 210, 235 *hpf* (hours post fertilization; Table 1) were obtained by *in vitro* fertilization following the method of Nagata and Miyabe (1978). Embryos were staged according to Yi et al. (2021). Embryos were incubated in a temperature-controlled incubator (22.5 ± 1 °C) and fixed in 3% paraformaldehyde (pFA) and 1% glutaraldehyde (GA). Digital microphotographs of fixed samples were obtained with a CCD (charge-coupled device) camera connected to stereo microscope (Nikon SMZ1500). For x-ray contrast enhancement, embryos were stained for at least 24 h in 0.3% phosphotungstic acid (PTA) dissolved in 70% ethanol. Samples were then brought back to 70% ethanol without PTA and mounted in low-melting point agarose for non-shift scanning in pipette tips.

Table 1 Sample information and microCT scanning parameters.

Age (hpf)	Stage name	Pixel size (µm)	Voltage (keV/W)	Exp. time (sec.)	Intensity
135	2-ovl	2.19	40/3	4	5000-9000
150	1-ovl	2.0615	40/3	4.5	5000-10000
165	1-ovl/pec-bud	0.9765	40/3	17	5000-8500
185	pec-bud	0.9989	80/7	3	5000-6300
210	high-pec	1.4582	40/3	9.5	5000-10000
235	long-pec	1.4299	40/3	8.5	5000-10000

Note: for each stage, we scanned at least two specimens. The stage names follow Yi et al. (2021). For the pec-bud stage at 185 hpf, we also tried a lower resolution scan with the voltage set to 40/3 keV/W. We found no practical difference in image quality between scans at 80/7 keV/W and 40/3 keV/W. Therefore, we decided to use the less time-consuming option for this stage, namely scanning with the higher voltage but shorter exposure time. Key: Dev, developmental; hpf, hours post fertilization; Exp, exposure; keV, kiloelectron volt.

MicroCT scanning

Attenuation-based microtomographic images were acquired using a Xradia 520 Versa 3D X-ray microscope (Zeiss), with the x-ray tube voltages source set at 80/7 or 40/3 keV/W (keV: kiloelectron volts). A thin LE1 filter was used to avoid beam hardening artifacts. During the CT scanning, the sample was placed on a rotation table and projection images are acquired over an angular range of 180 degree. To obtain high resolution images, a CCD (charge-coupled device) optical objective with 4x was applied in the scan. Images were acquired with voxel (volumetric 3D pixels after reconstruction) sizes of 1-1.5 µm, and tomographic reconstructions were made with the resident software (XMReconstructor). Reconstructed images were exported as TIFF and loaded into Avizo version 9.5 (Thermo Fisher Scientific) for 3D visualization.

3D visualization

The reconstructed volume was viewed "slice by slice" as virtual sections using the *Slice* module in the Avizo software (Version: 9.5; Thermo Fisher Scientific). A computational module *Resample transformed image* was applied to register images to the orthogonal direction of the anatomical axis. *Ortho View* was used for interactive orthogonal views in xy, yz and xz axis simultaneously. The *Volume endering* module was used for 3D view. Values of colormap and opacity degree were optimized in the settings of rendering. Scalebars were added using the *Scalebars* module.

Annotations on 2D slices

To generate a developmental atlas, serial virtual transverse sections were taken in rostrocaudal sequence from the olfactory bulb to the medulla oblongata. The section plane was settled parallel to the deep ventricular sulcus between telencephalon and diencephalon (the anterior intraencephalic sulcus or AIS). To keep a consistent prosomeric axis annotation, we visualize the transverse section from the rostral to caudal, the coronal section from dorsal to ventral, the sagittal section from medial to lateral along the general body axis (Figure 1f). Labels were added to each section in the Adobe InDesign software (Version: 15.0.2; Adobe Systems Inc., San José, California). For anatomical terms see the list of abbreviation. In general, and to facilitate cross-species comparisons, we adopted anatomical terms were adopted from the *Atlas of Early Zebrafish Brain Development* (Mueller and Wullimann, 2005, 2016).

Segmentation of brain ventricles

Segmentation of the brain ventricle was conducted in Avizo in two steps. First, a rough segmentation based on greyscale threshold was achieved semi-automatically and polished by using *Smooth labels* and *Remove islands* filters. These segmentation results were checked slice-by-slice and were correctified manually. The *Generate Surface* module was used to extract surfaces from the segmentation results. Brain ventricles were colored in yellow using the *Surface view* module, while the rest of the cranial tissues are in semi-transparent using the *Volume rendering* module. The segmented model of the brain ventricles was captured in dorsal, ventral, lateral, and rostral views and saved in TIFF format, annotated in Adobe InDesign.

Results

We have studied the developmental stages of 165, 185, 210, 235 *hpf* (hours post fertilization) of the brain in the rosy bitterling (*Rhodeus ocellatus*) using microCT. Throughout this study we have used the stage table of development of the rosy bitterling generated by Yi et al. (2021). To avoid confusion regarding the anatomical orientation, we follow Herget et al., (2014) and use the term rostral, caudal, dorsal and ventral as in classical descriptions for the linear axial system of the embryonic body. For the topological position, prosomeric position and considering the curved neuraxis, we use the terms anterior, posterior, alar and basal as alternatives (Figure 1f). The anterior and posterior of the transverse neuromeres has to regarding the bending neural axis. Our results are divided into two sections. First, we illustrated the development of the ventricular system. Second, we compiled a developmental atlas of the bitterling brain.

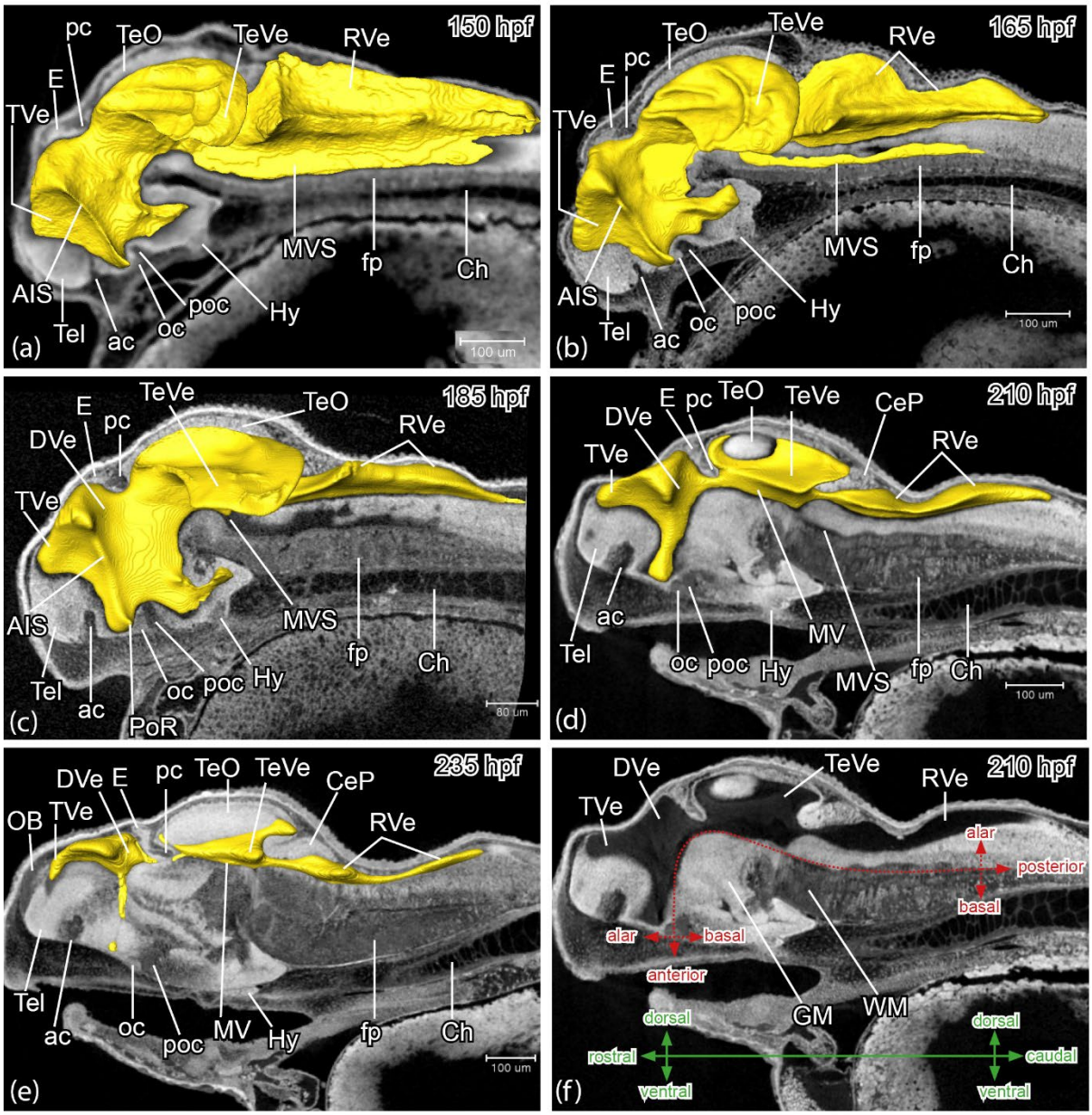

Figure 1 *Rhodeus ocellatus*, development of the brain ventricular system, microCT images, dorsal to the top, head to the left. (a-e) virtual midsagittal sections overlayed with surface view of manually-segmented brain ventricles, and showing the distinct ridge of the anterior intraencephalic sulcus (AIS) and progressive compartmentalization of the ventricular system (a-e). (f) virtual midsagittal section illustrating the black lumen of the brain ventricle, a bright white periventricular layer of gray matter (GM), and a gray peripheral layer of white matter (WM). The red dotted line indicates the neuraxis, with anterior, posterior, alar and basal topological direction for the curved axis. The green axes refer to the linear axial system apply to the brain parts with the terms rostral, caudal, dorsal, and ventral. The (a) stage 1-ovl, 150 hpf. (b) stage 1-ovl/pec-bud, 165 hpf. (c) stage pec-bud, 185 hpf. (d, f) stage high-pec, 210 hpf. (e) stage long-pec, 235 hpf. For annotations, see Table 2 List of Abbreviations. Scale bars = 100 µm (a, b, d, e. f); 80 µm (c).

A. Development of the brain ventricular system of the rosy bitterling

General description

The greyscale values we observed on virtual microCT sections depend on certain properties of the tissue such as dye precipitation, tissue density, and cell type. In the brain, the gray matter generally appeared brighter than the white matter (for example, compare the telencephalon and anterior commissure in Figure 1, Tel and ac). The white matter with its myelinated axons and tracts yielded greyscale values typical of low-density soft tissues (Figure 1, ac, poc, pc). In contrast, the brain ventricle, essentially a hollow space filled with cerebrospinal fluid (CSF), showed a lower density than the grey or white of the brain. It was visible in CT scans as the darkest part (Figure 1a-f, rendered in yellow color in Figure 1a-e). Therefore, the radiological appearance of the brain presented itself as a three-partitioned structure each separated by clear boundaries: (1) a black lumen (ventricle), (2) a bright white periventricular layer of gray matter, and (3) a gray peripheral layer of white matter (Figure 1f).

The forebrain ventricle divides dorsally by the position of the anterior intraencephalic sulcus (AIS) into the anterior telencephalic ventricle (TVe) and the posterior diencephalic ventricle proper (DVe or the 3rd ventricle; Figure 1). During the eversion of the telencephalic ventricle, the dorsal part of the AIS showed concomitant enlargement (Figure 1). Around the preoptic recess (PoR), the optic recess region (ORR) was recognizable, bordered by the anterior commissure (ac) and postoptic (poc) commissures (see locations of ac, poc and PoR in Figure 1c). The hypothalamic ventricle topographically locates caudal (topologically basal) to the optic recess region, and topologically anterior to the 3rd ventricle, including the lateral recess (LR) and the posterior recess (PR; Figure 2).

The lumen of the mesencephalon ventricle contains the paired tectal ventricle (TeVe), the median ventricle (MV), and the median ventricular sulcus (MVS) (Puelles, 2019). The TeVe projects dorsolaterally from the median ventricle (Figure 3a), covered by the subarea of the alar plate of the midbrain (optic tectum). A transiently visible median ventricular sulcus (MVS) branches off from the ventral bottom of the median ventricle and shows separately at the floor plate area (Figure 3b, inset in the upper right corner). The median ventricle extends caudally to the rhombencephalic ventricle (RVe or the 4th ventricle; Figure 3; García-Lecea et al., 2017; Korzh, 2018).

STAGE 1-ovl/pec-bud, 165 hpf.

In the rosy bitterling, the ventricular inflation is completed at stage 165 hpf (compare Figure 1a, b). The rhombencephalic ventricle (RVe) is diamond-shaped (rhombic) in dorsal and rostral aspects (Figure 3a and c). The bilateral tectal ventricles (TeVe) resemble scallop shells (Figure 3a). The telencephalic ventricle is triangular in rostral aspect (Figure 3d). A pair of oval fossae appear caudal-ventral to the midbrain (Figure 3c, of). These fossae are occupied by the rostral cerebellar thickenings, which develop into the valvula cerebelli of the adult (Wullimann and Knipp, 2000). The lateral recess (LR) and the posterior recess (PR) of the hypothalamic ventricle are in shallow groves (Figure 2a).

STAGE pec-bud, 185 hpf.

Width of the rhombencephalic ventricle (RVe) decreases to less than half of the tectal ventricles (TeVe) width (Figure 4a). The RVe gradually flattens along its dorsal-ventral axis (compare 3b and 4b). The dorsal surface of the TeVe appeared smoother due to a further developed optic tectum (mammalian superior colliculus) and torus semicircularis (mammalian inferior colliculus; Figure 4a).

There is a deep midline ridge separates left and right TeVe (Figure 4a, d). The preoptic recess (PoR) compressed, reduction in width (compare Figure 3c and 4c). The oval fossae enlarge with the growth of the rostral cerebellar thickening (compare Figure 3c and 4c). The lateral recess and posterior recess extend outward and become observable (Figure 2b).

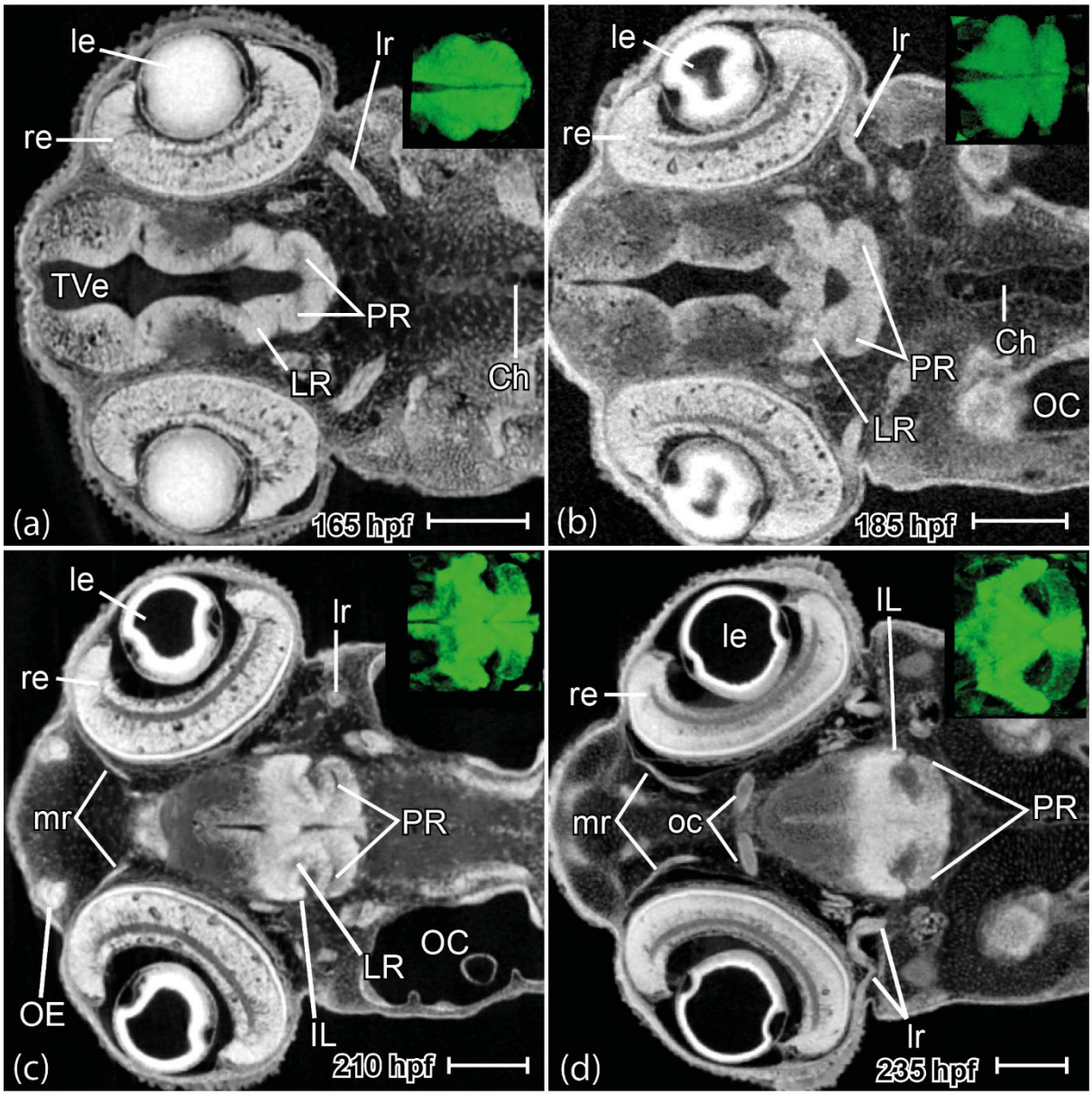

Figure 2 *Rhodeus ocellatus*, development of the lateral recess and posterior recess in the hypothalamus region. Virtual coronal sections, head to the left. At the right upper corner is the 3D volume rendering of the hypothalamus region seen from the dorsal side. (a) stage 1-ovl/pec-bud, 165 hpf. (b) stage pec-bud, 185 hpf. (c) stage high-pec, 210 hpf. (d) stage long-pec, 235 hpf. For annotations, see Table 2 List of Abbreviations. Scale bars = 100 µm.

STAGE high-pec, 210 hpf.

Compared to earlier stages, the brain ventricles appeared compressed at 210 hpf (compare Figure 4a and 5a). However, the dorsal ventricle of the anterior intraencephalic sulcus (AIS) appeared expanded probably due to the eversion of the telencephalic ventricle (TVe). The tectal lobes grow larger and adhesion between the right and left lobes emergent in the midline; therefore, the deep midline ridge of the TeVe appeared compressed rostrally (Figure 5b). The lateral recess (LR) extends

basalward to flange the posterior recess (PR), around the lateral recess forms the inferior lobe (IL, Figure 2c; Bloch et al. 2019).

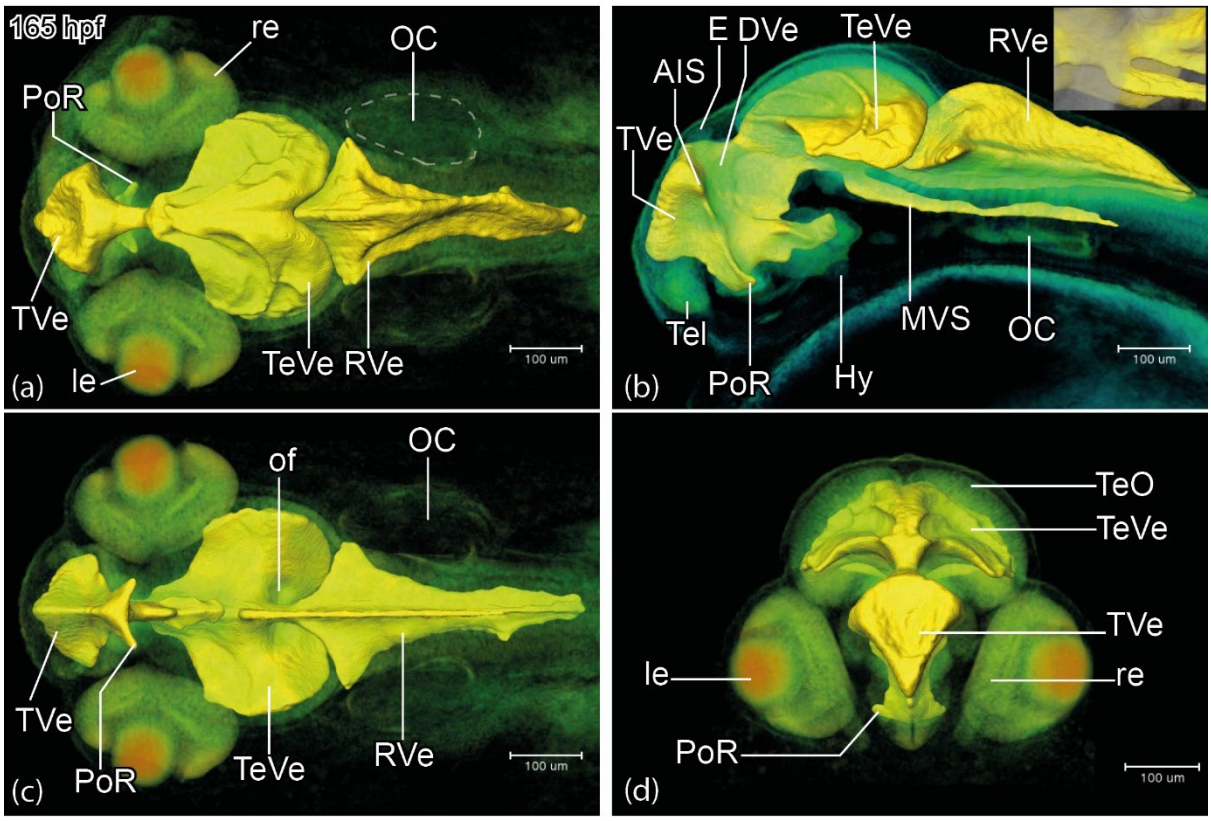

Figure 3 *Rhodeus ocellatus*, brain ventricular system at the stage 1-ovl/pec-bud, 165 hpf. (a-d) microCT images, the pseudo-colour volume rendering of the head region overlayed with a surface view of the manually-segmented brain ventricles. (a-d) dorsal, lateral, ventral, and rostral views, respectively. The inset in the upper right corner in (b) illustrates the median ventricular sulcus (MVS) branches off from the ventral bottom of the median ventricle of the mesencephalon. For annotations, see Table 2 List of Abbreviations. Scale bars = 100 µm.

STAGE long-pec, 235 hpf.

The rhombencephalic ventricle (RVe) can be divided into two portions, a rostral rhomboid opening with very thin roof plate tenting over, and a caudal elongated ventricle between the rhombic lips (RL; Figure 6a). The rostral view of the telencephalic ventricle (TVe) gradually deepens from a triangle into a T-shape (Figure 6d). Compared to earlier stages, the tectal ventricles (TeVe) are further compressed and separated from the median ventricle (Figure 6b). The lateral recess (LR) extends more basalward (compare Figure 2c and d), the inferior lobe (IL) enlarged considerable. The posterior recess (PR) extends alarward (Figure 2d).

B. Developmental atlas of the rosy bitterling brain

We noticed that there were cell clusters in periventricular locations that appeared brighter than the adjacent gray matter (eg. Figure 7j). The distribution of these cell clusters was highly consistent with the distribution of proliferation zones detected during neurogenesis in the zebrafish (Mueller and Wullimann, 2005, 2016). This fact has allowed us in this study to map proliferation zones of the developing bitterling brain and delineate brain territories. Therefore, the delineation of anatomical structures is based on three types of observation: (1) topological relationship to proliferation zones; (2) relative location to annotated brain ventricles (see previous section) and other landmarks such as

commissures and fiber tracts; (3) gray scale values in virtual slices. For example, the zona limitans intrathalamica (Zli) can be demarcated by its dark appearance from the surrounding bright white thalamic tissues (Figure 7g, h).

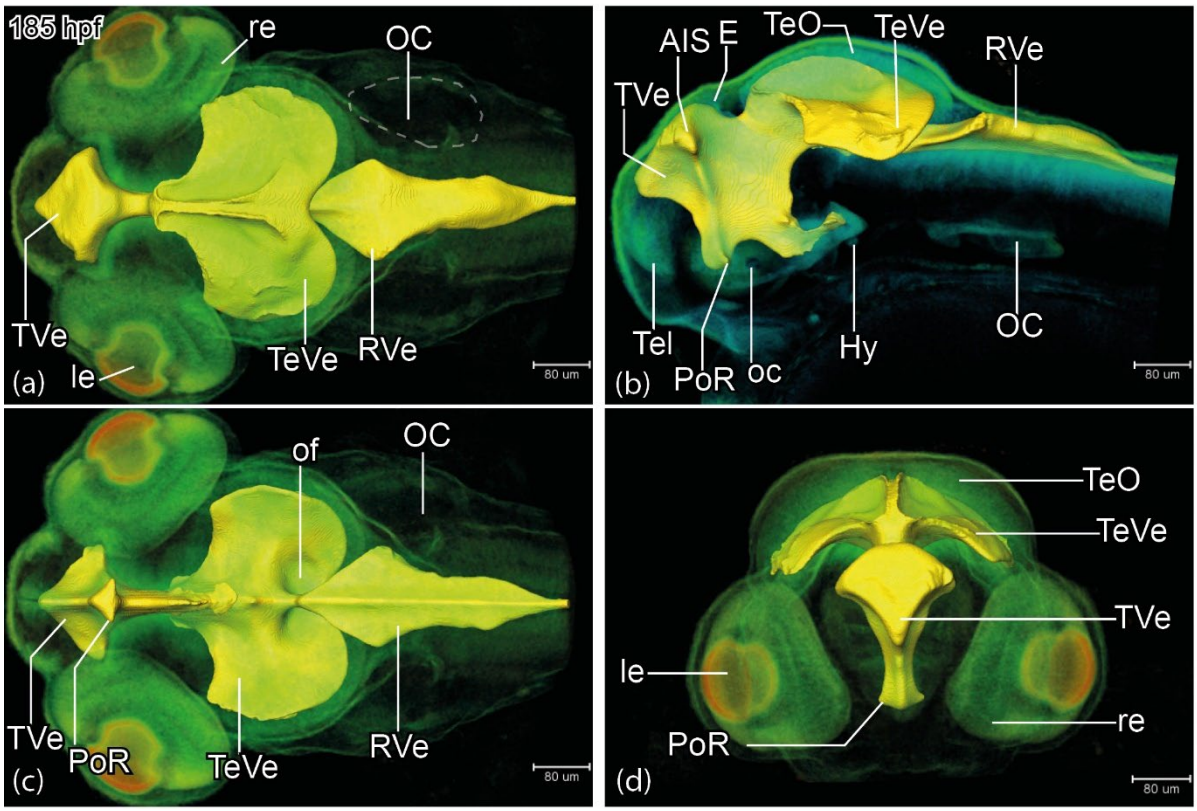

Figure 4 *Rhodeus ocellatus*, brain ventricular system at the stage pec-bud, 185 hpf. (a-d) microCT images, the pseudo-colour volume rendering of the head region overlayed with a surface view of the manually-segmented brain ventricles. (a-d) dorsal, lateral, ventral, and rostral views, respectively. For annotations, see Table 2 List of Abbreviations. Scale bars = 80 µm.

Secondary prosencephalon

Rostral to the telencephalic region, the olfactory epithelium (OE) is very bright, clearly visible from the 1-ovl/pec fin stage (165 hpf, Figure 7a). At the long-pec stage (235 hpf) the olfactory epithelium develops into a bow-shaped structure surrounding the lumen of the olfactory pits (Figure 10a). The olfactory epithelium (OE) is connected to the olfactory bulb (OB) through the easily recognizable olfactory nerve (ON; Figure 7c, 9b and 10b). The olfactory bulb (OB) is characterized by its glomerular structure (Figure 7a, 8a, 9a and 10a; Dynes and Ngai 1998).

The telencephalic ventricle is located at the dorsum of the pallium. The tela choroidea is in the roof of the ventricle. The periventricular proliferation zones of the subpallium (S) and pallium (P) in our samples appeared distinctively bright in virtual transverse sections. At the long-pec stage (235 hpf), the bright subpallial cell clusters were separated by distinct, dark boundaries (dashed line in Figure 10d), corresponding to the dorsal and ventral subdivisions of the subpallium (Sd and Sv). The

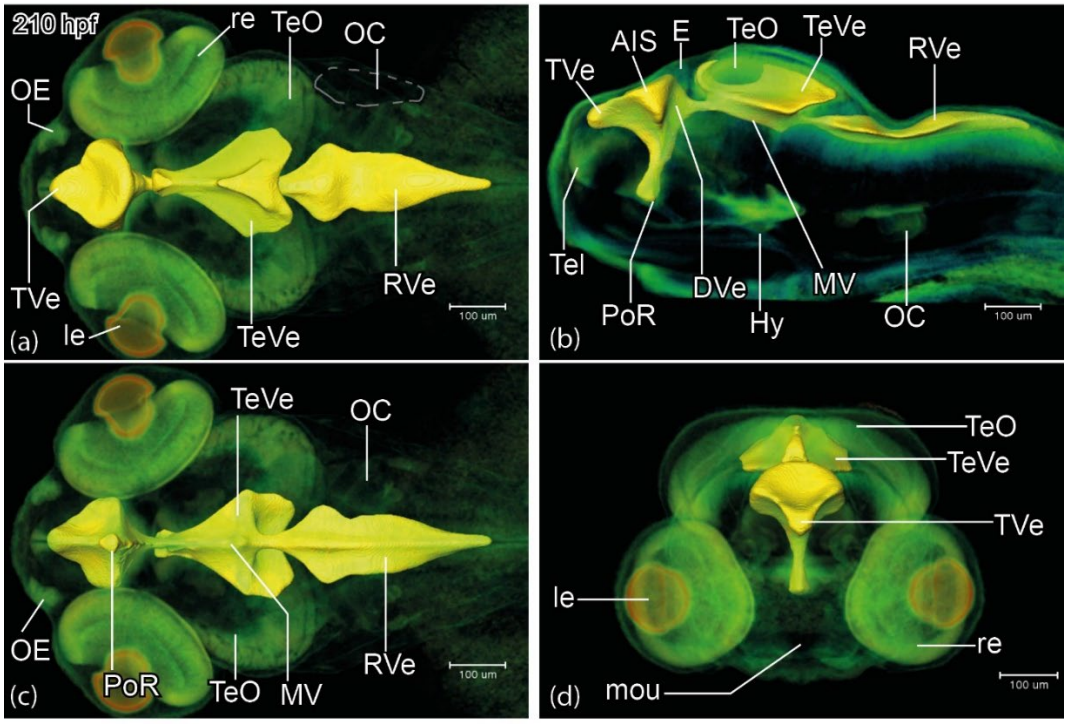

Figure 5 *Rhodeus ocellatus*, brain ventricular system at the stage high-pec, 210 hpf. (a-d) microCT images, the pseudo-colour volume rendering of the head region is overlayed with a surface view of the manually-segmented brain ventricles. (a-d) dorsal, lateral, ventral, and rostral views, respectively. For annotations, see Table 2 List of Abbreviations. Scale bars = 100 µm.

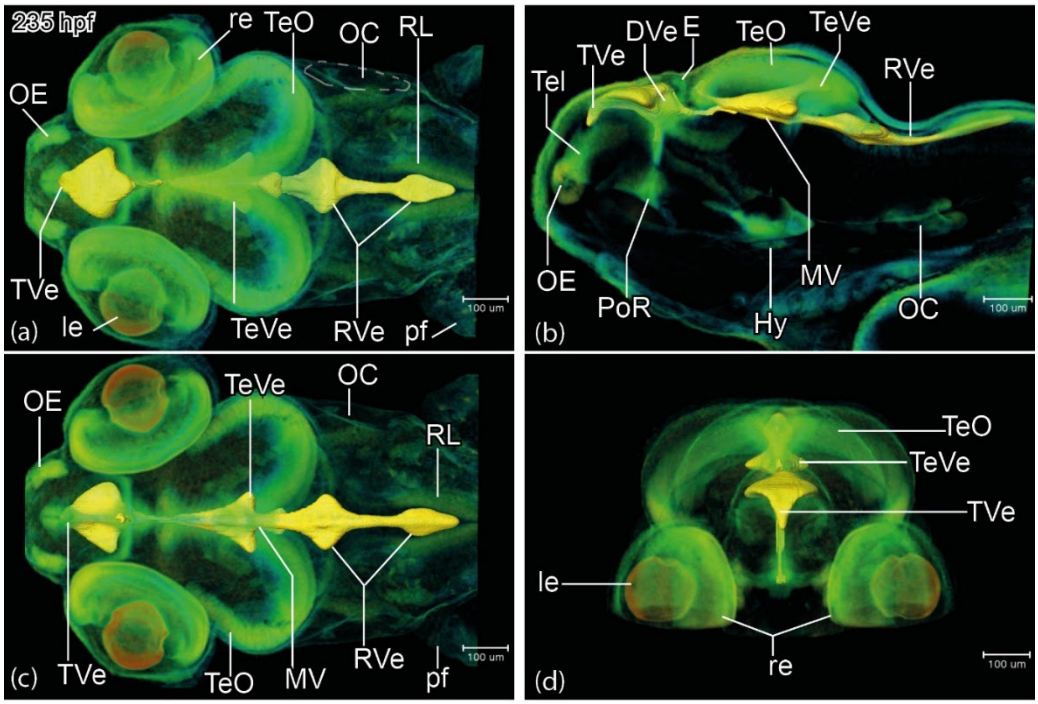

Figure 6 *Rhodeus ocellatus*, brain ventricular system at the stage long-pec, 235 hpf. (a-d) microCT images, the pseudo-colour volume rendering of the head region is overlayed with a surface view of the manually-segmented brain ventricles. (a-d) dorsal, lateral, ventral, and rostral views respectively. For annotations, see Table 2 List of Abbreviations. Scale bars = 100 µm.

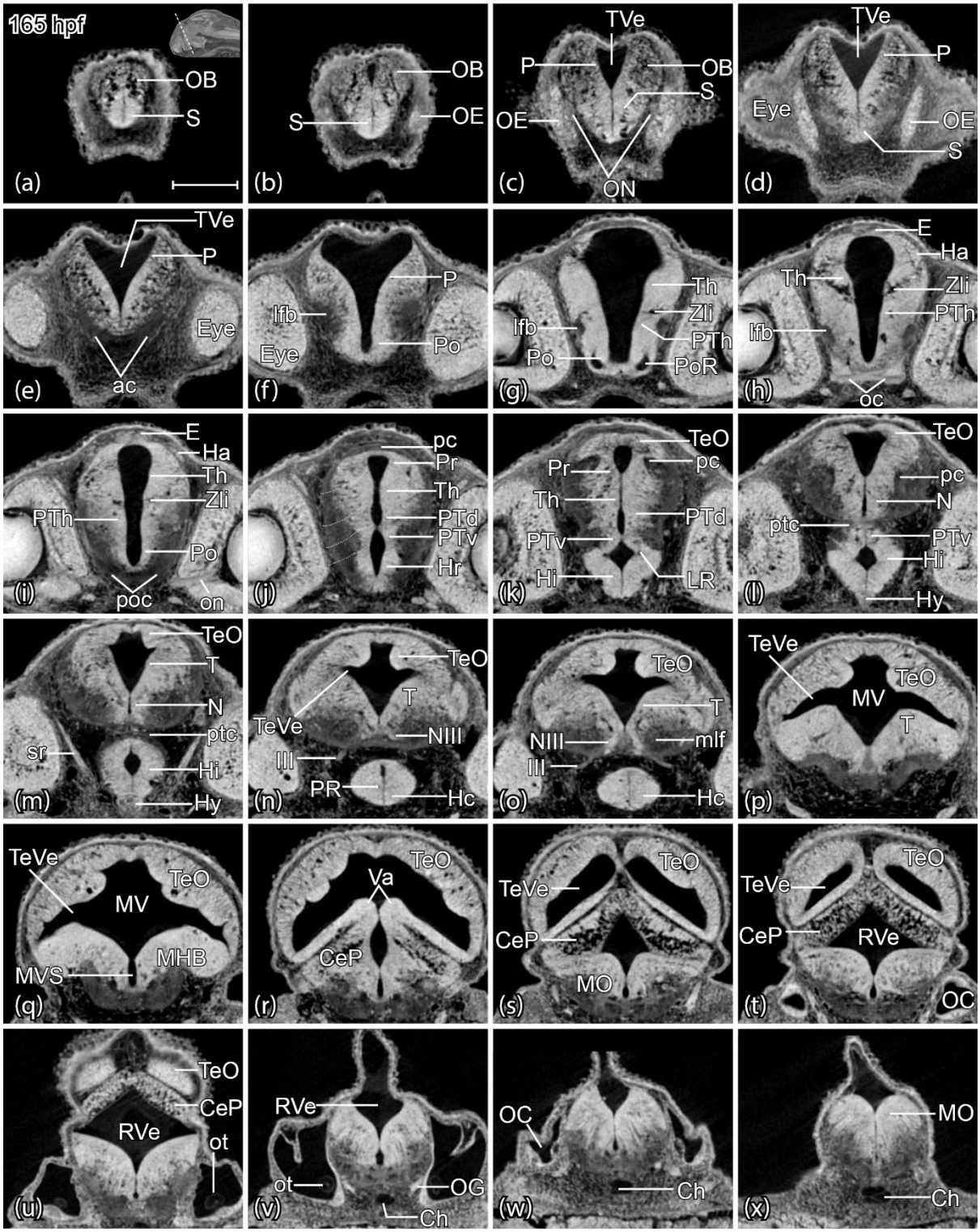

Figure 7 *Rhodeus ocellatus*, brain cross-sectional anatomy, stage 1-ovl/pec-bud, 165 hpf. (a-x) microCT images, virtual sections, transverse plane, dorsal towards the top, sections from rostral to caudal, direction of section plane indicated in inset in (a). For annotations, see Table 2 List of Abbreviations Scale bars = 100 µm.

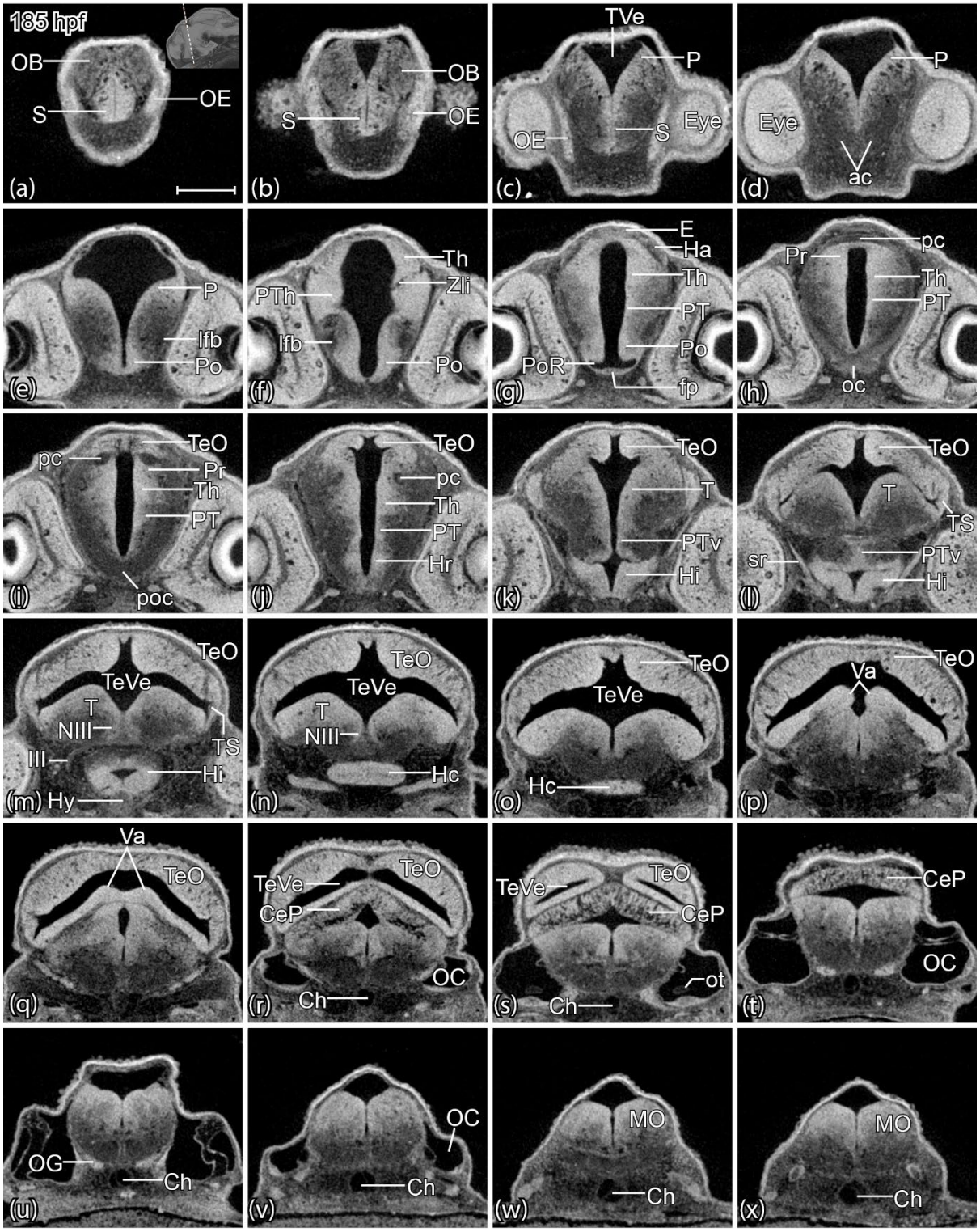

Figure 8 *Rhodeus ocellatus*, brain cross-sectional anatomy, stage pec-bud, 185 hpf. (a-x) microCT images, virtual sections, transverse plane, dorsal towards the top, sections from rostral to caudal, direction of section plane indicated in inset in (a). For annotations, see Table 2 List of Abbreviations. Scale bars = 100 µm.

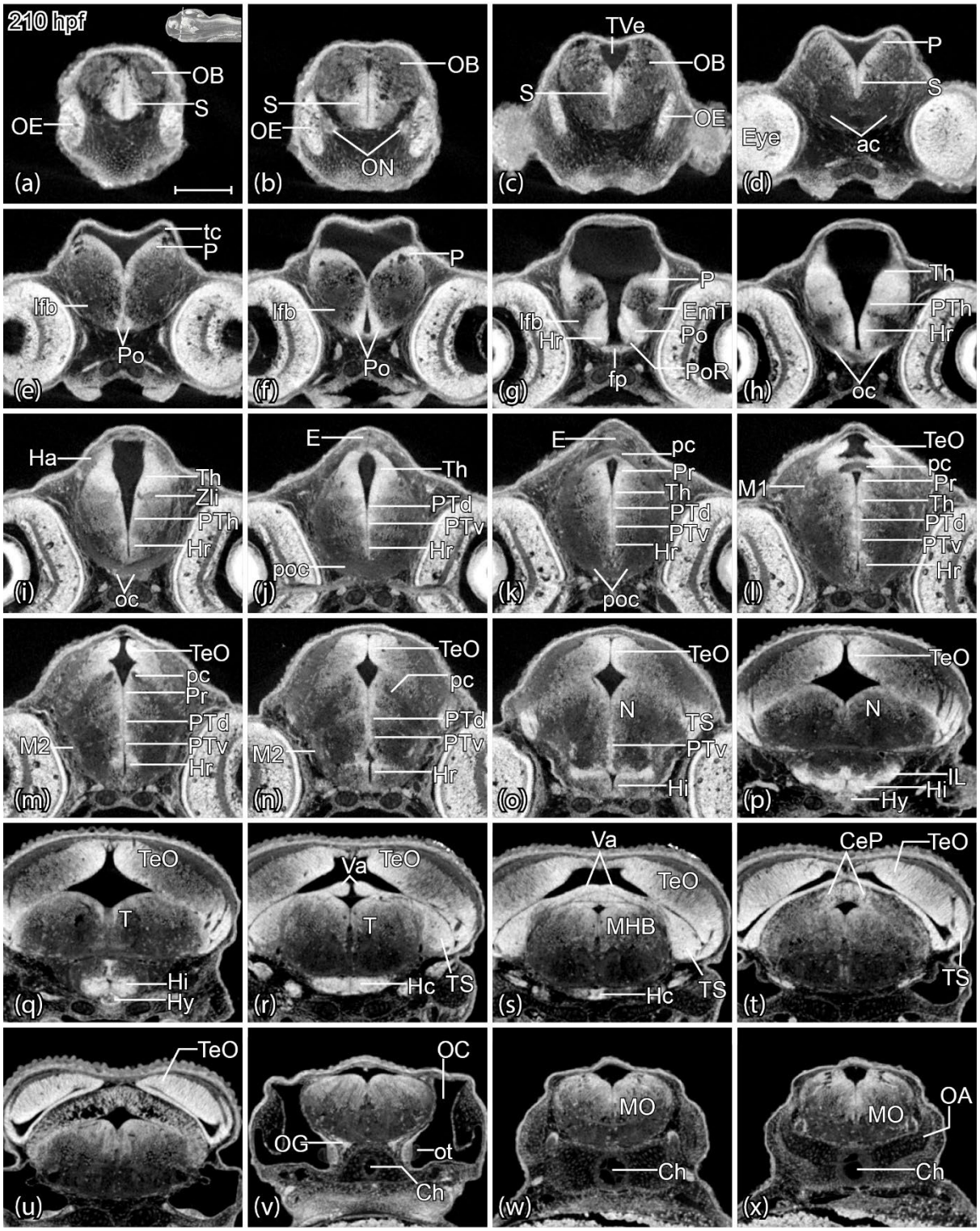

Figure 9 *Rhodeus ocellatus*, brain cross-sectional anatomy, stage high-pec, 210 hpf. (a-x) microCT images, virtual sections, transverse plane, dorsal towards the top, sections go from rostral to caudal, direction of section plane indicated in inset in (a). For annotations, see Table 2 List of Abbreviations. Scale bars = 100 µm.

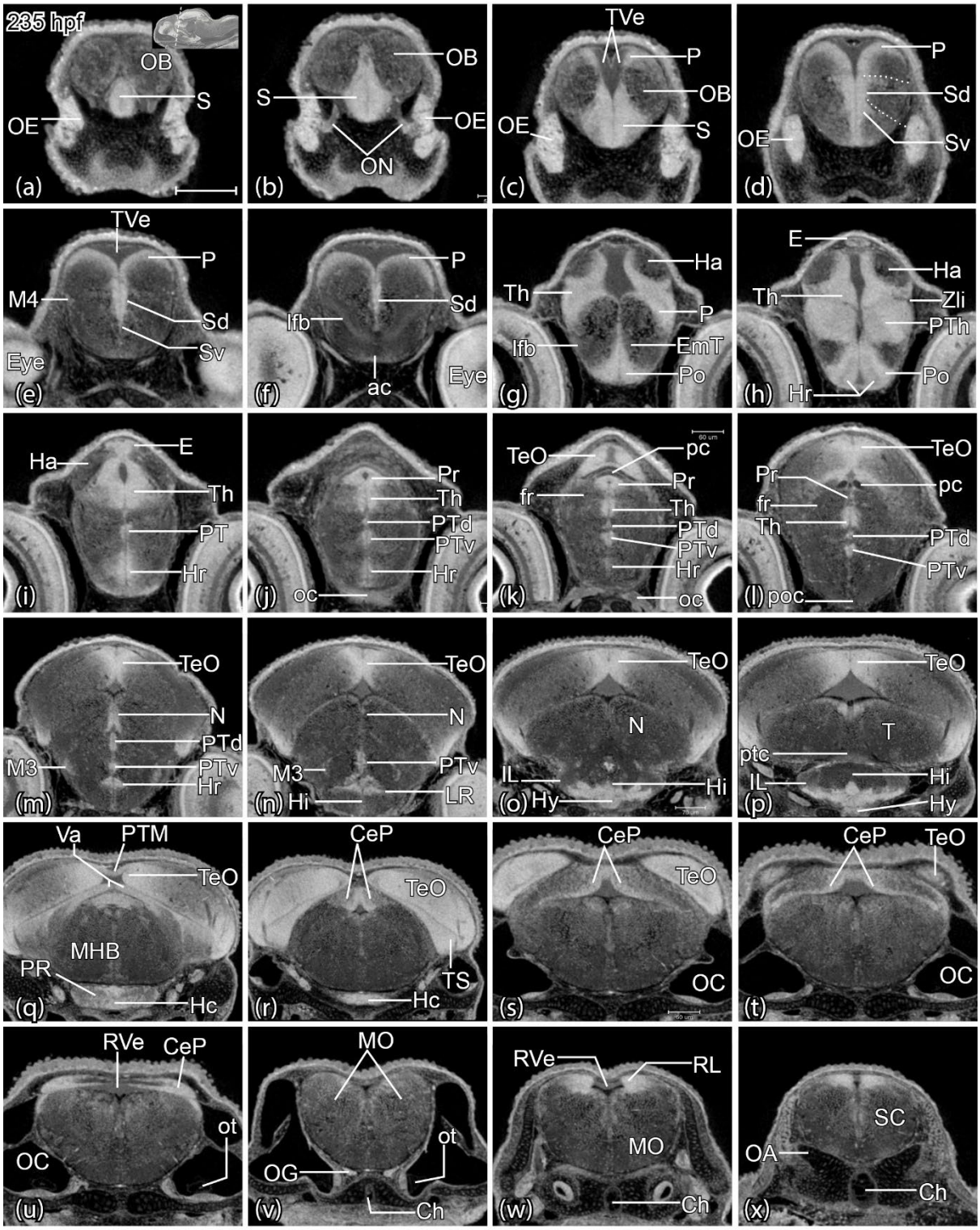

Figure 10 *Rhodeus ocellatus*, brain cross-sectional anatomy, stage long-pec, 235 hpf. (a-x) microCT images, virtual sections, transverse plane, dorsal towards the top, sections go from rostral to caudal, direction of section plane indicated in inset in (a). For annotations, see Table 2 List of Abbreviations. Scale bars = 100 µm.

zones of pallial proliferation consist of a few cell rows, and are visible as a pair of arches flanking the dorsal subpallium (Figure 7c, 8c, 9d, 10c). The telencephalic migrated area (M4) was recognizable as nonventricular proliferation cell clusters at the margin of the lateral subpallium (Figure 10e).

Immediately caudal to the subpallium, the anterior commissure (ac) and the lateral forebrain bundle (lfb) appeared as a dark fiber bundle crossing the rostral end of the forebrain (Figure 7e,f, 8d,e, 9d,e, 10f). We define the anterior commissure (ac) and the postoptic commissure (poc) as the boundaries of the preoptic region (Po) in this study. This region recently also has been considered he alar hypothalamus (aHyp) or the optic recess region (ORR) (Affaticati et al., 2015; Schredelseker and Driever, 2020; Slack, 2005). The proliferation zone of the preoptic region (Po) was easy to identify based on is triangular shape that surrounded the optic recess. The Po proliferation zone was broad on its ventral side and thins out dorsally (Figure 7f, 8e, 9e, 10g). The optic chiasma (oc) which has a bright, thick appearance, decussates in the midline (Figure 7h, 8h, 9h, 10j); it marks the anterior end of the neural axis.

In the basal hypothalamic region, the hypophysis topologically locates acroterminal (anterior) to the hypothalamus (Figure 2). It projects form the ventral midline of the brain (Figure 2). Like in the zebrafish developmental brain atlas, we divided the basal hypothalamus into the following regions: (i) the intermediate hypothalamus (Hi) near the hypophysis and including the inferior lobe (IL); (ii) the rostral hypothalamus (Hr) near the rostral end; and (iii) the caudal hypothalamus (Hc) near the caudal end. The hypothalamus encloses the hypothalamic ventricles including the lateral recess (LR) in the Hi and posterior recess (PR) in the Hc. This division is consistent with those classically used for describing the zebrafish hypothalamus (Wullimann et al., 1996; Manoli and Driever, 2014; Biran et al., 2015; Mueller and Wullimann, 2016; Muthu et al., 2016).

However, it should be noted that recent molecular studies in zebrafish improved the comparative interpretation of the teleostean hypothalamus and its evolutionary relationships with the mammalian hypothalamus (Baeuml et al., 2019; Herget et al., 2014). Likewise, gene expression in the PR tuberal region of embryonic zebrafish revealed homology with two domains of the mammalian hypothalamus, the TuV (tuberal region, ventral part) and TuI (tuberal region, intermedia part). Therefore, Schredelseker and Driever (2020) proposed to refer to this region as PRR (posterior recess region) to show its teleost specific phylogeny. Due to the fact, that our analysis in the rosy bitterling is based on purely anatomical microCT data, however, we were not able to relate our findings with those recent ones. For this purpose, future studies are required that analyze appropriate gene expression patterns in bitterlings.

Diencephalon

The prosomeric model divides the diencephalon, from caudal to rostral, into alar and basal plate derivatives. In this model, the pretectum (aP1), the thalamus proper (aP2), and the prethalamus (aP3) form the alar plate portions of the diencephalon (Lauter et al., 2013). In contrast, the proliferation zones of the nucleus of the medial longitudinal fasciculus (N; bP1), and the dorsal (bP2) and ventral (bP3) posterior tegmentum (PT; Mueller and Wullimann, 2005, 2016) form the corresponding basal plate derivatives.

Along the roof plate of the diencephalon, the most prominent structure is the epiphysis (E), a swelling in the dorsal midline of the brain (Figure 7h, 8g, 9j, 10i). The habenular nuclei (Ha) are located one each side of it (Figure 7h, 8g, 9i, 10i) and show discrete cell clusters from the pec-bud stage (185 hpf) onwards (Figure 8g). Notice that the fasciculus retroflexus (fr) appeared in our microCT photographs in the form of distinctive, dark fiber-bundles in the gray matter (Figure 10k, i). It originates from the habenular nuclei and connects to the interpeduncular nucleus across isthmus (r0) and rhombomere 1 (Akle et al., 2012). In the prosomeric model, the fasciculus retroflexus is used to delimit pretectum (P1) and thalamus (P2; Akle et al., 2012; Lauter et al., 2013; Puelles, 2019). We use the caudal end of the posterior commissure as the caudal boundary of the pretectum (P1), which divides the diencephalic area and the mesencephalic area (Figure 7j, 8h, 9l, 10k)

In the thalamic region, we identified the zona limitans intrathalamica (Zli) as a dark band (Figure 7i, 8f, 9i, 10h) that marks out the boundary between prethalamus (P3) and thalamus (P2). Therefore, we annotated the separate periventricular proliferation zones of prethalamus (PTh) and thalamus (Th) in the transverse virtual section based on their topological relationships (anterior vs. posterior) and Zli landmark (e.g., Figure 10j).

The thalamic eminence (EmT) is a relatively complex region of in the diencephalon and most often viewed in the prosomeric model as anterior portion of the prethalamus (hence often termed “prethalamic eminence”, PThE). However, while the EmT (or PThE) generates glutamatergic derivatives, the prethalamus proper forms predominantly GABAergic territories. In addition, some recent studies in zebrafish and tetrapods indicated that the Emt/PThE contributes to telencephalic territories such as the medial extended amygdala and newly identified nucleus of the lateral olfactory tract (Alonso et al., 2020; Porter and Mueller, 2020; Vicario et al., 2017). Due to the lack of molecular expression patterns, we stayed conservative in our analyses and placed the EmT topologically anterior to the prethalamus and posterior to the preoptic region similar as has been described for larval zebrafish (Wullimann and Mueller, 2004). It abuts the lateral forebrain bundle (Mueller, 2012) which is identifiable in our CT scans (Figure 7f, 8e, 9e, 10f). Molecular markers such as Tbr-1 are needed to validate our annotations (Wullimann, 2009; Wullimann and Mueller, 2004).

Note that the PT has distinct PTd and PTv proliferation zones (eg. Figure 10k). The neural axis is flexed here (i.e., at the cephalic flexure) and so the dorsal-ventral topology, in the virtual transverse sections, actually corresponds to the anterior-posterior axis of the neural tube.

Mesencephalon and rhombencephalon

The boundary between the diencephalon and mesencephalon defined dorsally by the posterior end of the posterior commissure and ventrally by anterior margin of the oculomotor nerve root (Moreno et al., 2016). In the tegmentum, we were able to identify the oculomotor nerve (III), which typically projects ventrolaterally from the oculomotor nucleus (NIII) and exits at the ventral surface of the brain (e.g., Figure 7n and o). The proliferation cluster of the oculomotor nucleus (NIII), and the basal plate of the mesencephalon, are thereby demarcated.

In the prosomeric model, the mesencephalon contains two mesomeres, m1 and m2 from anterior to posterior. the tectal gray, optic tectum (mammalian superior colliculus), and torus semicircularis (mammalian inferior colliculus) constitute thealar plate of m1. The oculomotor nucleus (NIII) represents the basal plate of m1.

We noticed two pairs of tectal membrane thickenings which invaginate into the tectal ventricle toward the tegmentum at the 1-ovl/pec-bud stage on 165 hpf (Figure 7q and r). During development, the boundaries between these thickenings gradually disappears as they growth together (Figure 8o and 9o). The tectal proliferation zones are distinct. At the 1-ovl/pec-bud stage (165 hpf) and the pec-bud stage (185 hpf), the tectal region appears as a large, bright field with the microCT (Figure 7o and 8l). Beginning with the high-pec stage (210 hpf), the rostral tectal proliferation becomes restricted to one mediodorsal cluster and two bilateral clusters (Figure 9o and 10n). These lateral and medial proliferation zones merge in the midline at caudal levels and form a continuous cap of tectal proliferation (e.g., Figure 9t).

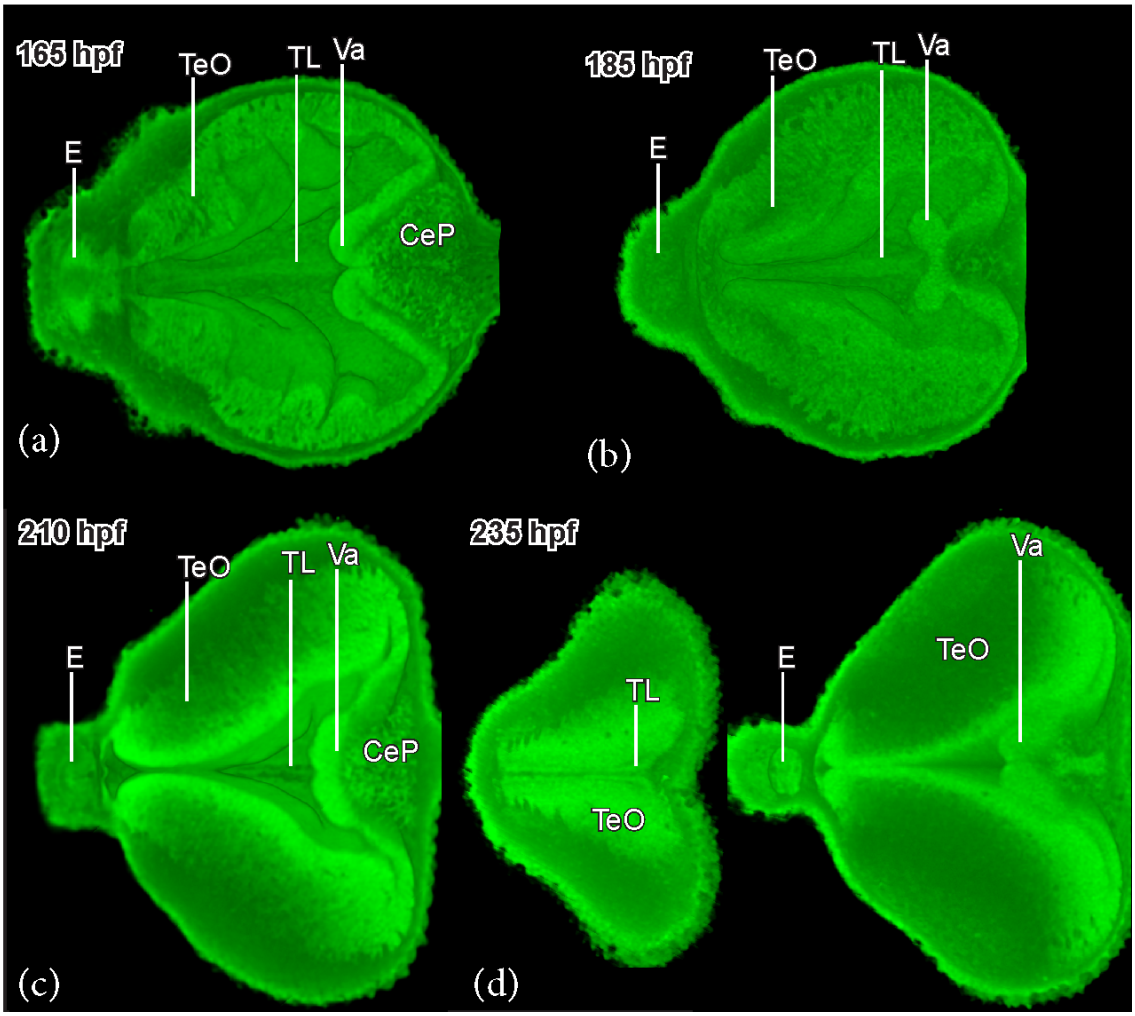

Figure 11 *Rhodeus ocellatus*, development of the torus longitudinalis. Virtual dissection, head to the left. (a) stage 1-ovl/pec-bud, 165 hpf. (b) stage pec-bud, 185 hpf. (c) stage high-pec, 210 hpf. (d) stage long-pec, 235 hpf. For annotations, see Table 2 List of Abbreviations.

The torus longitudinalis (TL) is a specialized brain region exclusive to ray-finned fish (Folgueira et al., 2020; Wullimann, 1994). We identified the TL from rostral to caudal along the medial margins of the optic tectum. Virtual horizontal sections through the optic tectum horizontally from the level of epiphysis and the rostral cerebellar thickening, revealed the TL can be seen at the top of the mesencephalic ventricle (Figure 11).

The r0, or isthmus, is at the midbrain-hindbrain boundary (MHB) region. The MHB is composed of the posterior tectal membrane and the rostral cerebellar thickenings (the valvula cerebelli; Wullimann and Knipp, 2000); appeared bright throughout the developmental period (Figure 7r, 8q, 9r, 10q). The cerebellar plate appeared bright only at its basal and medial aspects (e.g., Figure 10t and u). The trochlear nucleus (NIV) topologically belongs to r0. It is easier to identify the trochlear decussation (DIV) and the commissure cerebelli (Ccer) in the midsagittal section (Figure 12a-d) in the valvula cerebelli (Va). Then follow the caudolaterally projection of the trochlear axon in the horizontal section (Figure 12e) until it exits the brain as the trochlear nerve (IV, Figure 12f) between torus semicircularis and rhombencephalon. The axon tract of the trochlear nucleus delineates the boundary between r0 and r1.

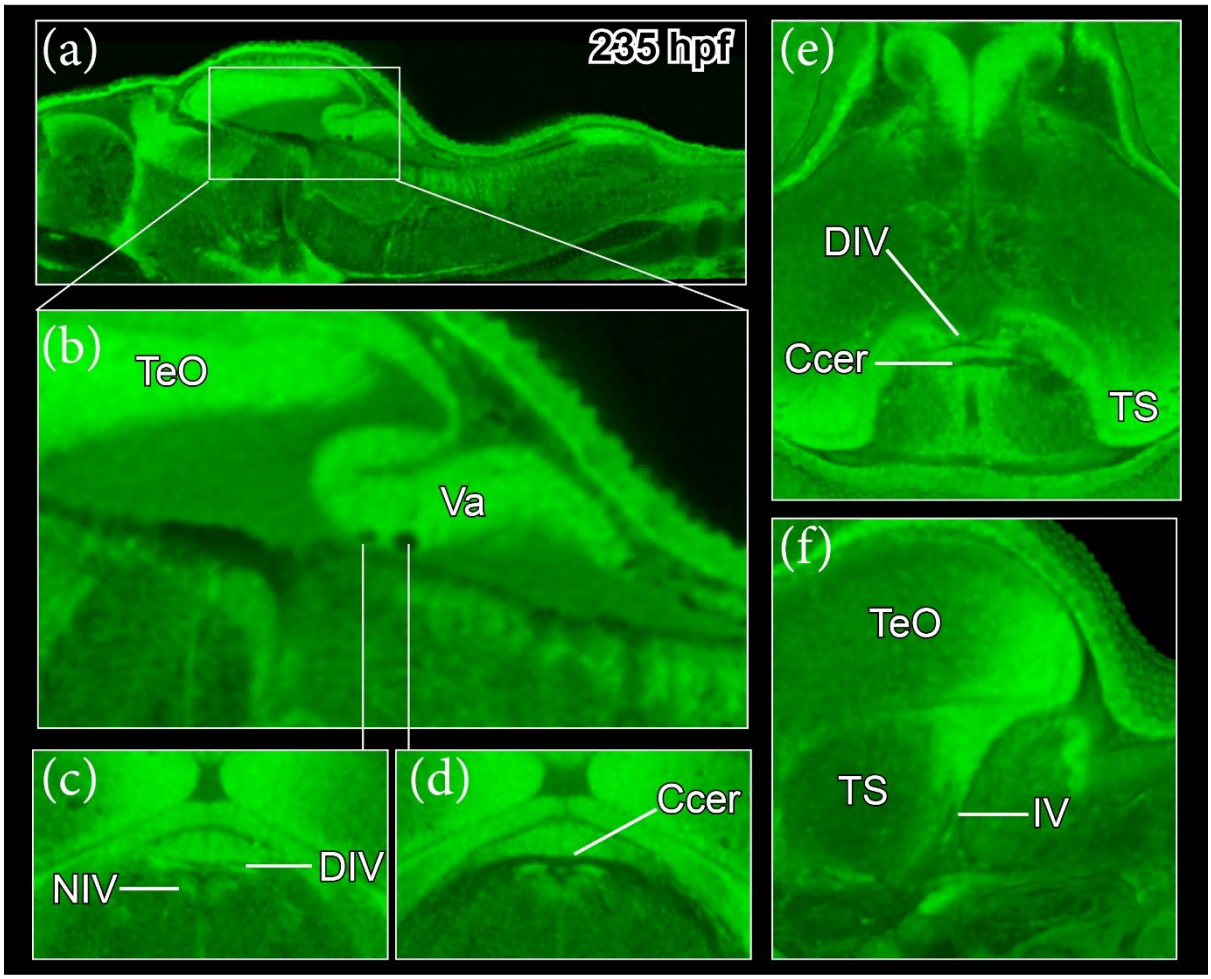

Figure 12 *Rhodeus ocellatus*, trochlear nerve, stage long-pec, 235 hpf. (a-f) microCT images, virtual sections. (a and b) midsagittal plane, head to the left, dorsal towards the top. (c and d) transverse plane, dorsal towards the top. (e) horizontal plane, head towards the top. (f) parasagittal plane, head to the left, dorsal towards the top. For annotations, see Table 2 List of Abbreviations.

The fasciculus retroflexus (fr) of teleosts innervates the interpeduncular nucleus (NIn). Thus, we used the white matter tract of the fr to identify the NIn in the bitterling embryo (Figure 13a). According to Lorente-Cánovas et al. (2012), the interpeduncular nucleus is at the basal plate across isthmus (r0) and r1. The r1 is devoid of cranial motor neurons (Nieuwenhuys and Puelles, 2016), therefore, we used the posterior margin of the interpeduncular nucleus as a landmark for the boundary between r1 and r2.

In the more caudal rhombencephalic region, the roof plate is a thin layer of tela choroidea, which is visible in microCT scans because it remains intact during the procedure (e.g., Figure 7x). The dorsal medullary proliferation zone is broad and expands ventrally up to the high-pec stage on 210 hpf (Figure 7v, 8v, and 9v), but at the long-pec stage (235 hpf) it becomes more restricted, forming the rhombic lip proliferation zone (Figure 10w).

The boundaries between rhombomeres from r2 to r8 are visible in early bitterling embryos at 135 hpf (Figure 14), but soon become less visible at least from the 1-ovl/pec fin stage at 165 hpf. However, teleost fish retain a segmented pattern of reticulospinal neurons through embryonic to adult (Gilland et al., 2014). For example, the large bilateral Mauthner neurons (M) is the marker of r4 (Eaton and Farley, 1973; Moens and Prince, 2002). By slicing the embryo of 135 hpf at the transverse level of r4, it is determined that the Mauthner cell reside near the central of rhombomere 4 rather than at the segmental boundaries (Figure 14). The rhombomeric segments of the older embryo (235 hpf, Figure 13a to k) were thereby identified by assuming that each reticulospinal neuronal cluster is located in the center of each rhombomeres.

The nerve roots of the cranial nerves are also reliable landmarks of rhombomeres. By tracing the projection of cranial nerves, we identified the trigeminal nerve root (V) in r2 (Figure 13e), the facial (VII) and the accompanying vestibulo-cochlear nerves in r4 (Figure 13g), the abducens root (VI) in r5 (Figure 13h), the glossopharyngeal root (IX) in r7 (Figure 13j), and the vagus root (X) in r8 (Figure 13k). The r2 was also labeled by somata of the anterior trigeminal motor neuron (NVa, Figure 13e) and the r3 by the posterior trigeminal motor neuron (NVp, Figure 13f). The facial motor neuron (NVII) is distinct in r6 (Figure 13i).

DISCUSSION

Brain imaging and 3D visualization of neuroanatomy

To gain insight into the complex morphogenesis of the bitterling brain, we analyzed the formation of the brain ventricular system in 3D from the stage 1-ovl (150 hpf) to long-pec (235 hpf) of bitterling development. We combined annotations of brain functional subdivisions and morphological landmarks, based on microCT scanning results and on the literature for the zebrafish embryo. We found that 3D visualization with microCT scanning protocols were extremely useful for the study of the rosy bitterling and provide an updating of imaging modalities for morphological and anatomical analyses in this non-model organism. A systematic application of microCT may help provide an essential foundation for future comparative studies of the teleost brain.

Our study provides 3D reconstruction of brain ventricles in the bitterling, showing similar organization to the zebrafish larval ventricular system as visualized by dye-injection into the hindbrain ventricle (Lowery and Sive, 2005). We have also defined boundaries of brain ventricle subdivisions based on published anatomical landmarks (Turner et al., 2012). Furthermore, we found that the flexure of the neuraxis is easily visualized continuously from the rostral tip of the brain to the spinal cord. Understanding the cephalic flexure is crucial because it has a drastic effect on the topology of the brain, especially in the highly complex secondary prosencephalon (Hauptmann and Gerster, 2000; Puelles, 2019). It has been shown that the mechanism of brain ventricle development is highly con-

versed across vertebrate (Lowery and Sive, 2009). The cerebrospinal fluid in the brain ventricular system could contribute to specialization of the early brain because the production and flow of cerebrospinal fluid performs an important role in homeostasis of the central nervous system (Fame et al., 2016).

In contrast to other vertebrates, actinopterygian fish like teleosts lack a pair of lateral ventricles in the telencephalon (Wullimann and Rink, 2002). Instead, they show a T-shaped midline telencephalic ventricle that is the result of a morphogenetic process called 'eversion' (Mueller and Wullimann, 2009). Our 3D models showed that in the rosy bitterling, the anterior intraencephalic sulcus (AIS) develops much earlier than the eversion of the telencephalic ventricle, and expansion of the dorsal ventricular surface of the AIS is synchronous with the eversion process. Our results are consistent with the telencephalic ventricle morphogenesis described in zebrafish (Folgueira et al., 2012). Initially, we could visualize the generation of the deep ventricular sulcus (AIS); followed by an anterolateral eversion of the telencephalic neuroepithelium.

We found distinct periventricular cell clusters in the gray matter with higher greyscale values than the surrounding tissue. Their distribution pattern was highly consistent with the distribution of proliferation zones described during neurogenesis of zebrafish (Mueller and Wullimann, 2003; Mueller and Wullimann, 2016; Mueller et al., 2006; Wullimann, 2009; Wullimann and Knipp, 2000; Wullimann and Mueller, 2004). It is possible, for example, that newly postmitotic neurons appear brighter than most of the postmitotic cell masses in more peripheral positions, remote from the periventricular proliferation zones. The result of immunohistochemistry for the neurotransmitter GABA (γ-aminobutyric acid) in zebrafish (Mueller and Wullimann, 2016; Mueller et al., 2006; Panganiban and Rubenstein, 2002), and PCNA (proliferation cell nuclear antigen) for proliferation patterns (Wullimann and Knipp, 2000; Wullimann and Mueller, 2004; Wullimann and Puelles, 1999) are consistent with our interpretation of the proliferation zones.

This study will hopefully pave the way to more detailed analyses of the bitterling brain. We hope that it will also prove valuable in studies using the growing number of fish models (and even non-fish models). Application of microCT 3D imaging provides a heuristic model of the brain, an extremely complex anatomical region. Importantly, our approach is validated by the fact that the profile of CT values displayed here in the bitterling brain are consistent with genoarchitecture identified in previous neurodevelopmental studies. For example, our annotation of the zona limitans intrathalamica (ZLI) is extremely close to the highly conserved expression pattern of the gene sonic hedgehog (*shh*; Vieira et al., 2005; Mueller et al., 2006; Scholpp et al., 2006). In addition, microCT allows time-efficient imaging of intact brains while providing a resolution (micron level) sufficient for displaying critical landmarks, groups of neurons such as proliferation zones versus postmitotic cell masses and white matter tracts. These histological characteristics are critical for detecting landmarks and visualize structural features as means to describe developmental neuroanatomy. However, the resolution of microCT is inferior to light microscopy of either histological brain sections or light sheet microscopy-based imaging of fluorescence-stained intact brains. It is also lower resolution than Synchrotron imaging, whose resolution reaches the sub-micron level, and therefore permits quantitative histological phenotyping (Ding et al., 2019). Neurons and neuropils in the central nervous system can be selectively stained with the salts of metallic elements including gold, silver, platinum and mercury chloride

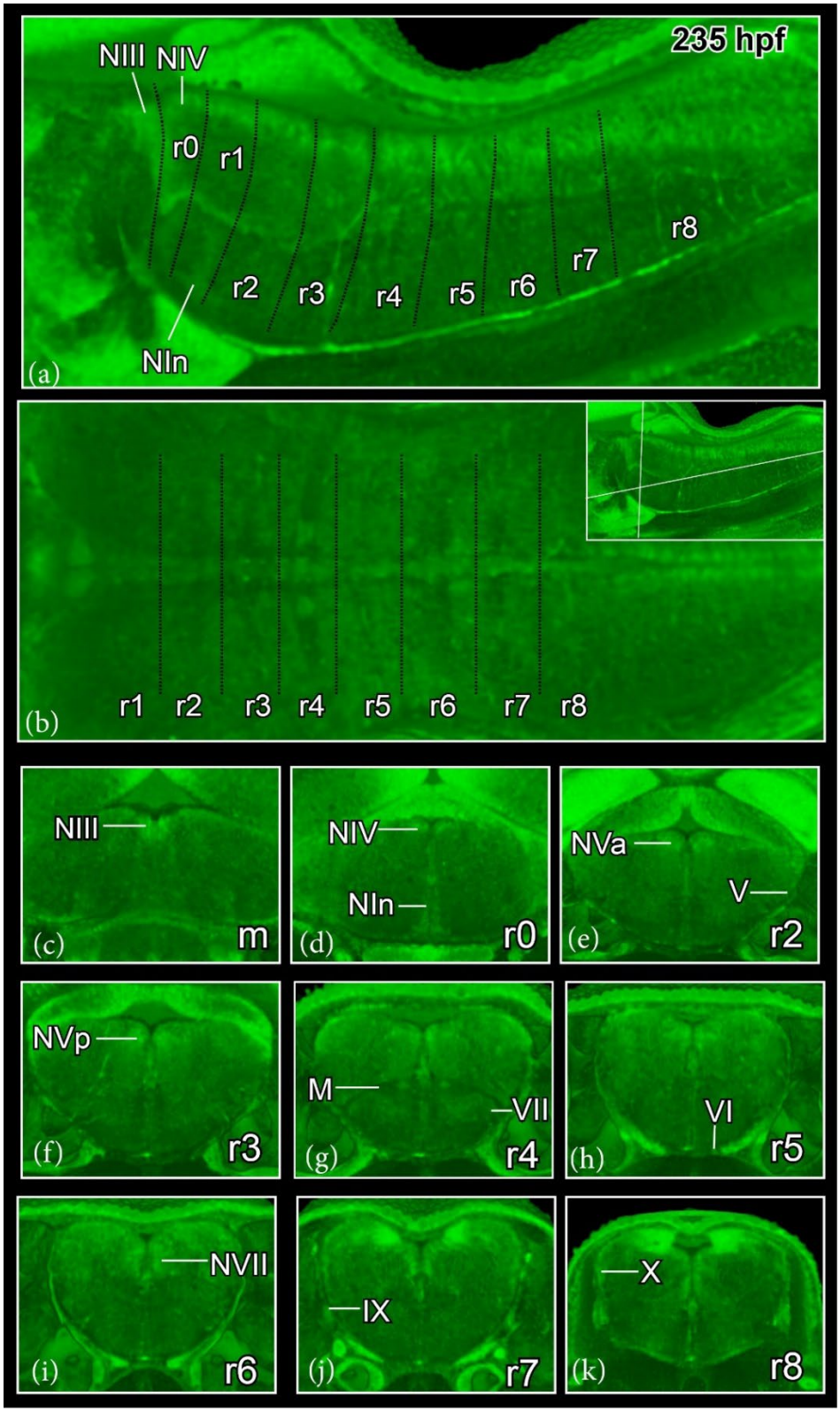

Figure 13 *Rhodeus ocellatus*, hindbrain segmentation, stage long-pec, 235 hpf. (a) microCT images, virtual sections, midsagittal plane, dorsal towards the top, head to the left. The black dash line indicates the rhombomeric boundaries. (b) horizontal plane, head to the left, direction of section plane indicated in inset at the upper right corner. (c-k) transverse plane, dorsal towards the top, sections go from the rostral to caudal, direction of section plane indicated in inset in (b). For annotations, see Table 2 List of Abbreviations.

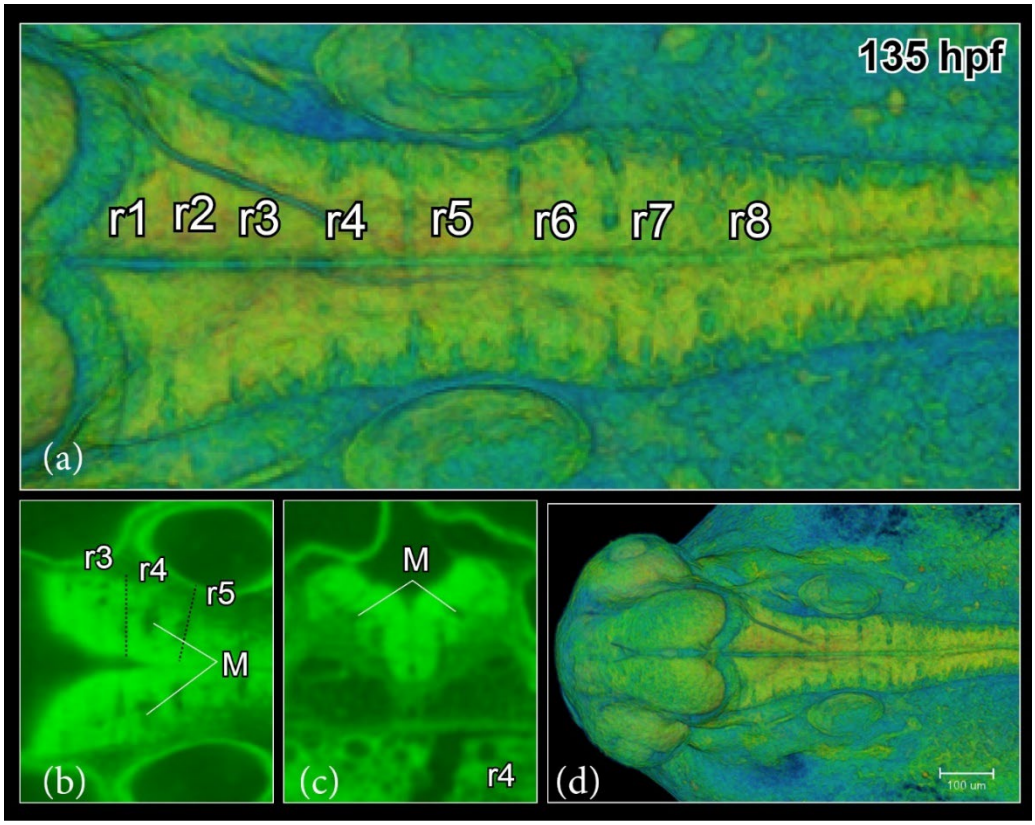

Figure 14 *Rhodeus ocellatus*, hindbrain segmentation, 135 hpf. (a and d) microCT images, volume rendering, show boundaries between rhombomeres. (b) virtual section, horizontal plane, head to the left, show the location of the Mauthner cell at the centre of r4. (c) virtual section, transverse plane, dorsal towards the top. For annotations, see Table 2 List of Abbreviations.

(Keklikoglou et al., 2019; Mizutani and Suzuki, 2012), which can compensate for the inability to use antibodies in combination with microCT. In summary, MicroCT imaging produces lower resolution than some imaging modalities, but has the special advantage that complex 3D models can be produced without the need for time-consuming reconstruction from histological material. The specimens imaged with microCT can be subsequently run through paraffin histology if needed.

Comparison of developmental stages between bitterling and zebrafish

The phylogenetic relationship of the rosy bitterling and the well-studied zebrafish are very close (Cypriniformes: Cyprinidae; Mayden et al., 2009). It allows for a relatively straight forward interspecies comparison of their brain development. The process of brain ventricle inflation, flexion of the neuroaxis, and establishment of prosomeric units, happens in bitterling as the same as in the zebrafish. Specifically, the 165 hpf bitterling brain and 30 hpf zebrafish brain are in the same process of brain ventricle inflation and have a similar degree of flexion of the neuroaxis. We noticed stratification of the proliferation zones of the diencephalic region (Pr, Th, PTd, PTv) is consistent between the 185 hpf bitterling brain and 36 hpf zebrafish brain.

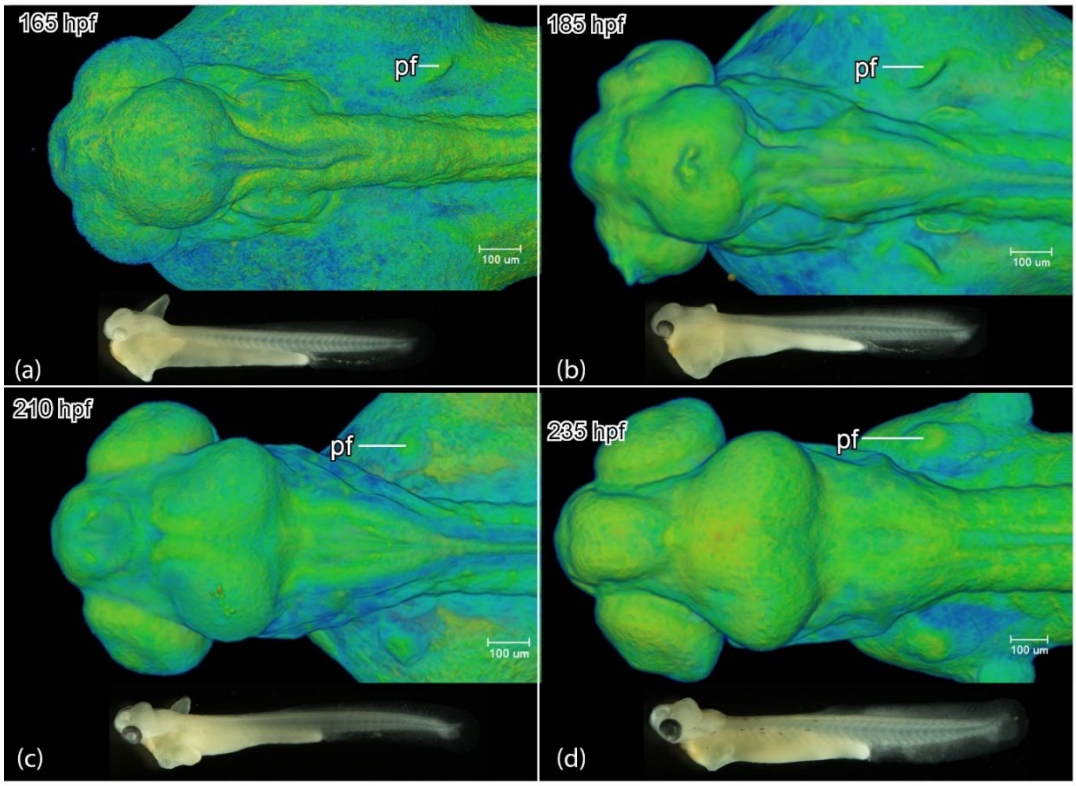

Figure 15 *Rhodeus ocellatus*, development of the brain region and the pectoral fin bud. Dorsal view of the head region microCT images, pseudo-colored volume-renderings, rostral to the left. Lateral view of the embryo, photomicrographs, rostral to the left. (a) 1-ovl/pec-bud, 165 hpf; (b) pec-bud, 185 hpf; (c) high-pec, 210 hpf; (d) long-pec 235 hpf. For annotations, see Table 2 List of Abbreviations.

However, distinct developmental heterochronies detected between bitterling and zebrafish brains. The bitterling shows precocious development of the inferior lobe and basalward extension of the lateral recess in the hypothalamic region (Figure 2): the inferior lobe is remarkable so early at the long-pec stage (235 hpf in bitterling, Figure 15; 48 hpf in zebrafish). The long-pec stage is defined by the development of the pectoral fin bud, when the pectoral fin bud of both species grows significantly to the distal end, and the bud height grows to twice of the width at the bud base (Kimmel et al., 1995; Yi et al., 2021). In zebrafish, the inferior lobe has not developed at the long-pec stage; it is identifiable until 5 days post fertilization (Bloch et al., 2019). In teleost fish, the inferior lobe is known as a multisensory integration center that involved in gustatory (Rink and Wullimann, 1998; Wullimann, 2020), visual (Butler et al., 1991), and octavolateralis system (Yang et al., 2007). Further studies can use the detailed descriptions of the bitterling brain developmental atlas provided here, to uncover the underlying regulatory mechanisms that control such heterochronic development.

Table 2 List of Abbreviations

Abbreviation	Anatomical terms
ac	anterior commissure
AIS	anterior intraencephalic sulcus
Ccer	commissure cerebelli
CeP	cerebellar plate
Ch	notochord
DIV	trochlear decussation
DVe	diencephalic ventricle
E	epiphysis
EmT	eminentia thalami
fp	floor plate
fr	fasciculus retroflexus
GM	gray matter
Ha	habenula
Hc	caudal hypothalamus
Hi	intermediate hypothalamus
Hr	rostral hypothalamus
Hy	hypophysis
III	oculomotor nerve
IL	inferior lobe of hypothalamus
IV	trochlear nerve
IX	glossopharyngeal nerve
le	lens
lfb	lateral forebrain bundle
LR	lateral recess of hypothalamic ventricle
lr	lateral rectus muscle
M	Mauthner neurons
M1	pretectal migrated area
M2	posterior tubercular migrated area
M3	EmT migrated area
M4	telencephalic migrated area
MHB	midbrain-hindbrain boundary
mlf	medial longitudinal fascicle
mou	mouth
MV	median ventricle of the mesencephalic ventricle
MVS	median ventricular sulcus of the mesencephalic ventricle
N	region of the nucleus of the medial longitudinal fascicle
NIII	oculomotor nucleus
NIn	interpeduncular nucleus
NIV	trochlear nucleus
NVa	rostral trigeminal motor neuron
NVII	facial motor neuron
NVp	caudal trigeminal motor neuron
OA	occipital arch
OB	olfactory bulb
oc	optic chiasma
OC	otic capsule
OE	olfactory epithelium
of	oval fossae
OG	octaval ganglion (VIII)
ON	olfactory nerve
on	optic nerve
ot	otolith
P	pallium
pc	posterior commissure
pf	pectoral fin
Po	preoptic region
poc	postoptic commissure
PoR	preoptic recess
PR	posterior recess of hypothalamic ventricle
Pr	pretectum
ptc	posterior tubercular commissure
PTd	dorsal part of posterior tuberculum
PTh	prethalamus
PTM	posterior tectal membrane
PTv	ventral part of posterior tuberculum
r	rhombomere
re	retina
RL	rhombic lip
RVe	rhombencephalic ventricle
S	subpallium
SC	spinal cord
Sd	dorsal subpallium
sr	superior rectus muscle
Sv	ventral subpallium
T	midbrain tegmentum
tc	tela choroidea
Tel	telencephalon
TeO	tectum opticum
TeVe	tectal ventricle
Th	thalamus
TL	torus longitudinalis
tpc	tract of posterior commissure
TS	torus semicircularis
TVe	telencephalic ventricle
V	trigeminal nerve
Va	valvula cerebeli
VI	abducens nerve
VII	facial nerve
WM	white matter
X	vagus nerve
Zli	zona limitans intrathalamica

References

Affaticati, P., Yamamoto, K., Rizzi, B., Bureau, C., Peyriéras, N., Pasqualini, C., Demarque, M. and Vernier, P. (2015). Identification of the optic recess region as a morphogenetic entity in the zebrafish forebrain. *Sci. Rep.* **5**, 8738.

Akle, V., Guelin, E., Yu, L., Brassard-Giordano, H., Slack, B. E. and Zhdanova, I. V. (2012). F-Spondin/spon1b Expression Patterns in Developing and Adult Zebrafish. *PLoS One* **7**, e37593.

Aldridge, D. C. (1999). Development of European bitterling in the gills of freshwater mussels. *J. Fish Biol.* **54**, 138–151.

Alonso, A., Trujillo, C. M. and Puelles, L. (2020). Longitudinal developmental analysis of prethalamic eminence derivatives in the chick by mapping of Tbr1 in situ expression. *Brain Struct. Funct.* **225**, 481–510.

Babaei, F., Hong, T. L. C., Yeung, K., Cheng, S. H. and Lam, Y. W. (2016). Contrast-Enhanced X-Ray Micro-Computed Tomography as a Versatile Method for Anatomical Studies of Adult Zebrafish. *Zebrafish* **13**, 310–316.

Baeuml, S. W., Biechl, D. and Wullimann, M. F. (2019). Adult islet1 Expression Outlines Ventralized Derivatives Along Zebrafish Neuraxis. *Front. Neuroanat.* **13**, 19.

Bloch, S., Thomas, M., Colin, I., Galant, S., Machado, E., Affaticati, P., Jenett, A. and Yamamoto, K. (2019). Mesencephalic origin of the inferior lobe in zebrafish. *BMC Biol.* **17**, 22.

Boeseman, M. J., Van der Drift, J., Van Roon, J. M., Tinbergen, N. and Ter Pelkwijk, J. J. (1938). De bittervoorns en hun mossels. *Levende Nat.* **43**, 129–136.

Butler, A. B., Wullimann, M. F. and Northcutt, R. G. (1991). Comparative cytoarchitectonic analysis of some visual pretectal nuclei in teleosts. *Brain. Behav. Evol.* **38**, 92–114.

Cambronero, F. and Puelles, L. (2000). Rostrocaudal nuclear relationships in the avian medulla oblongata: A fate map with quail chick chimeras. *J. Comp. Neurol.* **427**, 522–545.

Chang, H. W. (1948). Life history of the common Chinese bitterling, *Rhodeus ocellatus*. *Sinensia* **19**, 12–22.

Ding, Y., Vanselow, D. J., Yakovlev, M. A., Katz, S. R., Lin, A. Y., Clark, D. P., Vargas, P., Xin, X., Copper, J. E., Canfield, V. A., et al. (2019). Computational 3D histological phenotyping of whole zebrafish by X-ray histotomography. *Elife* **8**, e44898.

Duyvené de Wit, J. (1955). Some results of investigations into the European Bitterling, *Rhodeus amarus* BLOCH. *Japanese J. Icthyology* **4**, 94–104.

Dynes, J. L. and Ngai, J. (1998). Pathfinding of olfactory neuron axons to stereotyped glomerular targets revealed by dynamic imaging in living zebrafish embryos. *Neuron* **20**, 1081–1091.

Eaton, R. C. and Farley, R. D. (1973). Development of the Mauthner Neurons in Embryos and Larvae of the Zebrafish, *Brachydanio rerio*. **1973**, 673–682.

Fame, R. M., Chang, J. T., Hong, A., Aponte-Santiago, N. A. and Sive, H. (2016). Directional cerebrospinal fluid movement between brain ventricles in larval zebrafish. *Fluids Barriers CNS* **13**, 11.

Folgueira, M., Bayley, P., Navratilova, P., Becker, T. S., Wilson, S. W. and Clarke, J. D. W. (2012). Morphogenesis underlying the development of the everted teleost telencephalon. *Neural Dev.* **7**, 32.

Folgueira, M., Riva-Mendoza, S., Ferreño-Galmán, N., Castro, A., Bianco, I. H., Anadón, R. and Yáñez, J. (2020). Anatomy and Connectivity of the Torus Longitudinalis of the Adult Zebrafish. *Front. Neural Circuits* **14**, 1–20.

García-Lecea, M., Gasanov, E., Jedrychowska, J., Kondrychyn, I., Teh, C., You, M.-S. and Korzh, V. (2017). Development of Circumventricular Organs in the Mirror of Zebrafish Enhancer-Trap Transgenics. *Front. Neuroanat.* **11**, 114.

Gilland, E., Straka, H., Wong, T. W., Baker, R. and Zottoli, S. J. (2014). A hindbrain segmental scaffold specifying neuronal location in the adult goldfish, *Carassius auratus*. *J. Comp. Neurol.* **522**, 2446–2464.

Hauptmann, G. and Gerster, T. (2000). Regulatory gene expression patterns reveal transverse and longitudinal subdivisions of the embryonic zebrafish forebrain. *Mech. Dev.* **91**, 105–118.

Herget, U., Wolf, A., Wullimann, M. F. and Ryu, S. (2014). Molecular neuroanatomy and chemoarchitecture of the neurosecretory preoptic-hypothalamic area in zebrafish larvae. *J. Comp. Neurol.* **522**, 1542–1564.

His Wilhelm (1895). *Die anatomische Nomenclatur. Nomina anatomica,*. Veit.

Keklikoglou, K., Faulwetter, S., Chatzinikolaou, E., Wils, P., Brecko, J., Kvaček, J., Metscher, B. and Arvanitidis, C. (2019). Micro-computed tomography for natural history specimens: a handbook of best practice protocols. *Eur. J. Taxon.* **522**, 1–55.

Kimmel, C. B., Ballard, W. W., Kimmel, S. R., Ullmann, B. and Schilling, T. F. (1995). Stages of embryonic development of the zebrafish. *Dev. Dyn.* **203**, 253–310.

Kitamura, J., Nagata, N., Nakajima, J. and Sota, T. (2012). Divergence of ovipositor length and egg shape in a brood parasitic bitterling fish through the use of different mussel hosts. *J. Evol. Biol.* **25**, 566–573.
Korzh, V. (2018). Development of brain ventricular system. *Cell. Mol. Life Sci.* **75**, 375–383.
Lauter, G., Söll, I. and Hauptmann, G. (2013). Molecular characterization of prosomeric and intraprosomeric subdivisions of the embryonic zebrafish diencephalon. *J. Comp. Neurol.* **521**, 1093–1118.
Lawrence, C. (2007). The husbandry of zebrafish (Danio rerio): A review. *Aquaculture*.
Liu, H. Z., Zhu, Y. R., Smith, C. and Reichard, M. (2006). Evidence of host specificity and congruence between phylogenies of bitterling and freshwater mussels. *Zool. Stud.* **45**, 428–434.
Lorente-Cánovas, B., Marín, F., Corral-San-Miguel, R., Hidalgo-Sánchez, M., Ferrán, J. L., Puelles, L. and Aroca, P. (2012). Multiple origins, migratory paths and molecular profiles of cells populating the avian interpeduncular nucleus. *Dev. Biol.* **361**, 12–26.
Lowery, L. A. and Sive, H. (2005). Initial formation of zebrafish brain ventricles occurs independently of circulation and requires the nagie oko and snakehead/atp1a1a.1 gene products. *Development* **132**, 2057–2067.
Lowery, L. A. and Sive, H. (2009). Totally tubular: the mystery behind function and origin of the brain ventricular system. *BioEssays* **31**, 446–458.
Ma, L. H., Punnamoottil, B., Rinkwitz, S. and Baker, R. (2009). Mosaic hoxb4a neuronal pleiotropism in zebrafish caudal hindbrain. *PLoS One* **4**, e5944.
Mayden, R. L., Chen, W.-J., Bart, H. L., Doosey, M. H., Simons, A. M., Tang, K. L., Wood, R. M., Agnew, M. K., Yang, L., Hirt, M. V., et al. (2009). Reconstructing the phylogenetic relationships of the earth's most diverse clade of freshwater fishes—order Cypriniformes (Actinopterygii: Ostariophysi): A case study using multiple nuclear loci and the mitochondrial genome. *Mol. Phylogenet. Evol.* **51**, 500–514.
Metscher, B. D. (2009a). MicroCT for comparative morphology: simple staining methods allow high-contrast 3D imaging of diverse non-mineralized animal tissues. *BMC Physiol.* **9**, 11.
Metscher, B. D. (2009b). MicroCT for developmental biology: a versatile tool for high-contrast 3D imaging at histological resolutions. *Dev Dyn* **238**, 632–640.
Mills, S. C. and Reynolds, J. D. (2003). The bitterling-mussel interaction as a test case for co-evolution. *J. Fish Biol.* **63**, 84–104.
Mizutani, R. and Suzuki, Y. (2012). X-ray microtomography in biology. *Micron* **43**, 104–115.
Moens, C. B. and Prince, V. E. (2002). Constructing the hindbrain: Insights from the zebrafish. *Dev. Dyn.* **224**, 1–17.
Moreno, N., Morona, R., López, J. M. and González, A. (2016). The Diencephalon and Hypothalamus of Nonmammalian Vertebrates: Evolutionary and Developmental Traits. In *Evolution of Nervous Systems: Second Edition*, pp. 409–426.
Mueller, T. (2012). What is the Thalamus in Zebrafish? *Front. Neurosci.* **6**, 64.
Mueller, T. and Wullimann, M. F. (2003). Anatomy of neurogenesis in the early zebrafish brain. *Dev. Brain Res.* **140**, 137–155.
Mueller, T. and Wullimann, M. F. (2009). An Evolutionary Interpretation of Teleostean Forebrain Anatomy. *Brain. Behav. Evol.* **74**, 30–42.
Mueller, T. and Wullimann, M. F. (2016). *Atlas of Early Zebrafish Brain Development*. Second edi. Elsevier.
Mueller, T., Vernier, P. and Wullimann, M. F. (2006). A phylotypic stage in vertebrate brain development: GABA cell patterns in zebrafish compared with mouse. *J. Comp. Neurol.* **494**, 620–634.
Nagata, Y. and Miyabe, H. (1978). Development Stages of the Bitterling, Rhodeus ocellatus ocellatus(Cyprinidae). *Mem. Osaka Kyoiku Univ. III, Nat. Sci. Appl. Sci.* **26**, 171–181.
Nieuwenhuys, R. and Puelles, L. (2016). *Towards a New Neuromorphology*. Cham: Springer International Publishing.
Noll, C. F. (1877). Gewohnheiten und Eierlegen des Bitterlings. *Zool. Garten* **18**, 351–379.
Olt, A. (1893). Lebensweise und Entwicklung des Bitterlings. *Zeitschrift für wissenschaftliche Zool.* **55**, 543–575.
Panganiban, G. and Rubenstein, J. L. R. (2002). Developmental functions of the Distal-less/Dlx homeobox genes. *Development* **129**, 4371–4386.
Porter, B. A. and Mueller, T. (2020). The Zebrafish Amygdaloid Complex – Functional Ground Plan, Molecular Delineation, and Everted Topology. *Front. Neurosci.* **14**, 608.
Puelles, L. (2019). Survey of Midbrain, Diencephalon, and Hypothalamus Neuroanatomic Terms Whose Prosomeric Definition Conflicts With Columnar Tradition. *Front. Neuroanat.* **13**, 20.
Puelles, L. and Rubenstein, J. L. R. (2003). Forebrain gene expression domains and the evolving prosomeric model. *Trends Neurosci.* **26**, 469–476.

Rahmat, S. and Gilland, E. (2019). Hindbrain neurovascular anatomy of adult goldfish (*Carassius auratus*). *J. Anat.* **235**, 783–793.
Reichard, M., Liu, H. and Smith, C. (2007). The co-evolutionary relationship between bitterling fishes and freshwater mussels: insights from interspecific comparisons. *Evol. Ecol. Res.* **9**, 239–259.
Richardson, M. K. and Wright, G. M. (2003). Developmental transformations in a normal series of embryos of the sea lamprey *Petromyzon marinus* (Linnaeus). *J. Morphol.* **257**, 348–363.
Rink, E. and Wullimann, M. F. (1998). Some forebrain connections of the gustatory system in the goldfish *Carassius auratus* visualized by separate DiI application to the hypothalamic inferior lobe and the torus lateralis. *J. Comp. Neurol.* **394**, 152–170.
Rouchet, R., Smith, C., Liu, H. Z., Methling, C., Douda, K., Yu, D., Tang, Q. Y. and Reichard, M. (2017). Avoidance of host resistance in the oviposition-site preferences of rose bitterling. *Evol. Ecol.* **31**, 769–783.
Schmitz, B., Papan, C. and Campos-Ortega, J. A. (1993). Neurulation in the anterior trunk region of the zebrafish Brachydanio rerio. *Roux's Arch. Dev. Biol.* **202**, 250–259.
Scholpp, S., Wolf, O., Brand, M. and Lumsden, A. (2006). Hedgehog signalling from the zona limitans intrathalamica orchestrates patterning of the zebrafish diencephalon. *Development* **133**, 855–864.
Schredelseker, T. and Driever, W. (2020). Conserved Genoarchitecture of the Basal Hypothalamus in Zebrafish Embryos. *Front. Neuroanat.* **14**, 3.
Slack, J. M. W. (2005). *Essential Developmental Biology (2nd ed.)*. Oxford, UK: BlackWell Publishing Ltd.
Smith, C. (2016). Bayesian inference supports the host selection hypothesis in explaining adaptive host specificity by European bitterling. *Oecologia* **183**, 1–11.
Smith, C., Reichard, M., Jurajda, P. and Przybylski, M. (2004). The reproductive ecology of the European bitterling (Rhodeus sericeus). *J. Zool.* **262**, 107–124.
Turner, M. H., Ullmann, J. F. P. and Kay, A. R. (2012). A method for detecting molecular transport within the cerebral ventricles of live zebrafish (*Danio rerio*) larvae. *J. Physiol.* **590**, 2233–2240.
Vernier, P. (2017). The Brains of Teleost Fishes. In *Evolution of Nervous Systems*, pp. 59–75. Elsevier.
Vicario, A., Mendoza, E., Abellán, A., Scharff, C. and Medina, L. (2017). Genoarchitecture of the extended amygdala in zebra finch, and expression of FoxP2 in cell corridors of different genetic profile. *Brain Struct. Funct.* **222**, 481–514.
Vieira, C., Garda, A. L., Shimamura, K. and Martinez, S. (2005). Thalamic development induced by Shh in the chick embryo. *Dev. Biol.* **284**, 351-363.
Wiepkema, P. R. (1962). An Ethological Analysis of the Reproductive Behaviour of the Bitterling (*Rhodeus Amarus* Bloch). *Arch. Néerlandaises Zool.* **14**, 103-199.
Wong, M. D., Van Eede, M. C., Spring, S., Jevtic, S., Boughner, J. C., Lerch, J. P. and Mark Henkelman, R. (2015). 4D Atlas of the Mouse Embryo for Precise Morphological Staging. *Dev.* **142**, 3583–3591.
Wullimann, M. F. (1994). The teleostean torus longitudinalis: A short review on its structure, histochemistry, connectivity, possible function and phylogeny. *Eur. J. Morphol.* **32**, 235–242.
Wullimann, M. F. (2009). Secondary neurogenesis and telencephalic organization in zebrafish and mice: a brief review. *Integr. Zool.* **4**, 123–133.
Wullimann, M. F. (2020). Neural origins of basal diencephalon in teleost fishes: Radial versus tangential migration. *J. Morphol.* **281**, 1133–1141.
Wullimann, M. F. and Knipp, S. (2000). Proliferation pattern changes in the zebrafish brain from embryonic through early postembryonic stages. *Anat. Embryol. (Berl).* **202**, 385–400.
Wullimann, M. F. and Mueller, T. (2004). Identification and Morphogenesis of the Eminentia Thalami in the Zebrafish. *J. Comp. Neurol.* **471**, 37–48.
Wullimann, M. F. and Puelles, L. (1999). Postembryonic neural proliferation in the zebrafish forebrain and its relationship to prosomeric domains. *Anat. Embryol. (Berl).* **199**, 329–348.
Wullimann, M. F. and Rink, E. (2002). The teleostean forebrain: A comparative and developmental view based on early proliferation, Pax6 activity and catecholaminergic organization. *Brain Res. Bull.* **57**, 363–370.
Yang, C.-Y., Xue, H.-G., Yoshimoto, M., Ito, H., Yamamoto, N. and Ozawa, H. (2007). Fiber connections of the corpus glomerulosum pars rotunda, with special reference to efferent projection pattern to the inferior lobe in a percomorph teleost, tilapia (*Oreochromis niloticus*). *J. Comp. Neurol.* **501**, 582–607.
Yi, W., Rücklin, M., Poelmann, R. E., Aldridge, D. C. and Richardson, M. K. (2021). Normal stages of embryonic development of a brood parasite, the rosy bitterling *Rhodeus ocellatus* (Teleostei: Cypriniformes). *J. Morphol.* **282**, 783–819.